Monthly Notices of the ROYAL ASTRONOMICAL SOCIETY

MNRAS **512,** 686–711 (2022) https://doi.org/10.1093/mnras/stac313
Advance Access publication 2022 February 7

AGN impact on the molecular gas in galactic centres as probed by CO lines

Federico Esposito [1,2]★ Livia Vallini [3] Francesca Pozzi,[1,2] Viviana Casasola [4] Matilde Mingozzi,[5] Cristian Vignali [1,2] Carlotta Gruppioni [2] and Francesco Salvestrini[6]

[1]*Dipartimento di Fisica e Astronomia, Università degli Studi di Bologna, Via P. Gobetti 93/2, I-40129 Bologna, Italy*
[2]*Osservatorio di Astrofisica e Scienza dello Spazio (INAF-OAS), Via P. Gobetti 93/3, I-40129 Bologna, Italy*
[3]*Scuola Normale Superiore, Piazza dei Cavalieri 7, I-56126 Pisa, Italy*
[4]*INAF – Istituto di Radioastronomia, Via P. Gobetti 101, I-40129 Bologna, Italy*
[5]*Space Telescope Science Institute, 3700 San Martin Drive, Baltimore, MD 21218, USA*
[6]*INAF – Osservatorio Astrofisico di Arcetri, Largo Enrico Fermi 5, I-50125 Firenze, Italy*

Accepted 2022 February 1. Received 2022 January 31; in original form 2021 November 17

ABSTRACT

We present a detailed analysis of the X-ray, infrared, and carbon monoxide (CO) emission for a sample of 35 local ($z \leq 0.15$), active ($L_X \geq 10^{42}$ erg s^{-1}) galaxies. Our goal is to infer the contribution of far-ultraviolet (FUV) radiation from star formation (SF), and X-ray radiation from the active galactic nuclei (AGNs), respectively, producing photodissociation regions (PDRs) and X-ray-dominated regions (XDRs), to the molecular gas heating. To this aim, we exploit the CO spectral line energy distribution (CO SLED) as traced by Herschel, complemented with data from single-dish telescopes for the low-J lines, and high-resolution ALMA images of the mid-J CO emitting region. By comparing our results to the Schmidt–Kennicutt relation, we find no evidence for AGN influence on the cold and low-density gas on kpc-scales. On nuclear ($r = 250$ pc) scales, we find weak correlations between the CO line ratios and either the FUV or X-ray fluxes: this may indicate that neither SF nor AGN radiation dominates the gas excitation, at least at $r = 250$ pc. From a comparison of the CO line ratios with PDR and XDR models, we find that PDRs can reproduce observations only in presence of extremely high gas densities ($n > 10^5$ cm^{-3}). In the XDR case, instead, the models suggest moderate densities ($n \approx 10^{2-4}$ cm^{-3}). We conclude that a mix of the two mechanisms (PDR for the mid-J, XDR, or possibly shocks for the high-J) is necessary to explain the observed CO excitation in active galaxies.

Key words: photodissociation region (PDR) – galaxies: active – galaxies: ISM.

1 INTRODUCTION

The molecular gas phase of the interstellar medium (ISM) is the fuel for star formation (SF), thus it plays a central role in galaxy evolution (McKee & Ostriker 2007; Carilli & Walter 2013; Tacconi, Genzel & Sternberg 2020). At the same time, the molecular gas properties (e.g. temperature, density, turbulence, chemical composition) are affected by feedback processes induced by SF and by the accretion on to the central black hole in sources hosting an active galactic nucleus (AGN; Aalto et al. 1995; Omont 2007; Imanishi et al. 2011; Imanishi, Nakanishi & Izumi 2016). A key question is whether, and on which spatial scales, the effect of AGN radiation on the molecular gas can produce observable effects that can be retrieved from the molecular-line emission.

Molecular hydrogen (H_2), dominating the mass of molecular ISM, does not have a dipole moment, and the quadrupole transitions require high temperatures ($T = 500$–2000 K), mainly present in shock-heated gas (Flower & Pineau Des Forêts 2010). For this reason, the most used molecular gas tracer is the carbon monoxide (CO), which has instead bright dipole emission and is the second most abundant molecule in the Universe (Bolatto, Wolfire & Leroy 2013).

Moreover, the CO Spectral Line Energy Distribution (CO SLED), i.e. the luminosity of CO rotational lines as a function of the rotational quantum number J,[1] is a very powerful diagnostic for the physical conditions of molecular ISM (Narayanan & Krumholz 2014; Rosenberg et al. 2015). The CO SLED can be broken down into three different parts (e.g. Vallini et al. 2019; Decarli et al. 2020). The low-J lines ($J_{upp} \leq 3$) trace the cold ($T \approx 20$–50 K), low-density ($n \lesssim 10^3$ cm^{-3}) gas; this is where the majority of the mass resides, so these lines are good tracers of the total molecular gas mass in galaxies (Bolatto et al. 2013). Both the mid-J ($4 \leq J_{upp} \leq 7$) and the high-J ($J_{upp} \geq 8$) lines originate from increasingly denser ($n \approx 10^4$–10^6 cm^{-3}) and warmer ($T \approx 100$–500 K) molecular gas (Greve et al. 2014). For this reason, the excitation of the CO ladder, especially in the mid/high-J part, can be exploited to disentangle different heating sources such as radiation from SF, AGN accretion, and mechanical heating from shocks (e.g. van der Werf et al. 2010; Mingozzi et al. 2018).

Stellar radiation affects the molecular gas mainly in the far-ultraviolet (FUV, $6 < h\nu < 13.6$ eV) band, where photons can dissociate H_2 molecules without ionizing H atoms (for which photons with $h\nu \geq 13.6$ eV are needed). The FUV photon penetration creates a transition layer, called photodissociation region (PDR), linking the outer H II region and the fully molecular layers of Giant Molecular

★ E-mail: federico.esposito7@unibo.it

[1]The CO SLED is also often referred to as the *CO rotational ladder*.

Clouds (GMCs). FUV-induced photoelectric effect on dust grains is the major heating mechanism in PDRs (Hollenbach & Tielens 1997, 1999), which then cool down through metal fine structure line emission (e.g. [C II] 158 μm, [O I] 63 μm) and molecular rotational lines, among which CO transitions. The FUV flux is usually parametrized in terms of the Habing field ($G_0 = 1.6 \times 10^{-3}$ erg s^{-1} cm^{-2}, Habing 1968).

X-ray photons from the AGN penetrate deeper than FUV photons into the molecular clouds and create the so-called X-ray-Dominated Regions (XDR; Maloney, Hollenbach & Tielens 1996). There, the heating and chemical composition of the gas are peculiarly influenced by the ∼1–100 keV X-ray radiation (Maloney et al. 1996; Meijerink & Spaans 2005; Meijerink, Spaans & Israel 2007), keeping the molecular gas warmer at larger (column) densities, following the release of fast photoelectrons (Morrison & McCammon 1983; Wilms, Allen & McCray 2000).

PDR and XDR models are radiative transfer calculations (Hollenbach & Tielens 1999; Meijerink et al. 2007; Ferland et al. 2017) that take the impinging radiation (FUV and X-ray photons, respectively), the gas density, column density, and metallicity as input, and return the expected line emission. While the low/mid-*J* CO emission is usually consistent with the presence of a PDR component produced by SF (Pereira-Santaella et al. 2013; Kamenetzky et al. 2014; Talia et al. 2018), in active galaxies with peculiarly excited high-*J* CO lines (van der Werf et al. 2010; Schleicher, Spaans & Klessen 2010; Gallerani et al. 2014; Pozzi et al. 2017; Vallini et al. 2019; Pensabene et al. 2021) an XDR, associated with the AGN activity, is often necessary to reproduce the CO SLEDs.

The purpose of this work is to investigate the possible relation between the AGN activity and the conditions of molecular gas in a sample of local active galaxies with well-sampled CO SLED. We will assess whether, and to what extent, the excitation of the CO ladder shows correlations with X-ray and FUV tracers and whether the CO SLED can be used to infer the effect of SF versus AGN heating on the whole host galaxy and within the nuclear region.

The paper is structured as follows. In Section 2, we introduce the sample and the selection criteria. In Section 3, we describe the data collection from the sub-mm up to the X-ray band. In Section 4, we derive the CO emission on a galactic scale, and we study the Schmidt–Kennicutt relation. In Section 5, we derive the physical parameters for the PDR and XDR analysis and we discuss the results we find. We assume a ΛCDM cosmology with $H_0 = 70$ km s^{-1} Mpc^{-1}, $\Omega_m = 0.3$, and $\Omega_\Lambda = 0.7$.

2 SAMPLE SELECTION

To investigate the impact of AGN activity on to the molecular gas, we select a sample of local galaxies adopting the following criteria: (i) a properly sampled CO SLED in the mid/high-*J* regimes from *Herschel* observations; (ii) an intrinsic 2–10 keV luminosity $L_X \geq 10^{42}$ erg s^{-1}. Moreover, we collect low/mid-*J* CO data by considering both sub-mm/mm single-dish observations, and interferometric ALMA data, which ensure a high spatial resolution.

Selecting sources with intrinsic $L_X \geq 10^{42}$ erg s^{-1} is the standard criterion for identifying AGN, since stellar processes alone (e.g. X-ray binaries, hot ionized ISM) rarely reach this X-ray luminosity (Hickox & Alexander 2018). We look for AGN with a well-sampled CO SLED, to be able to study the high-*J* lines ($J_{upp} \geq 8$), where we expect to find the imprint of the AGN influence on the molecular gas.

The adopted criteria lead to a sample of 35 active galaxies (see Table 1), with redshifts in the range $0.0015 < z < 0.15$ (median $z = 0.02$), corresponding to luminosity distances (D_L) in the range of 4−720 Mpc.

Considering the classification from the optical spectra, 92 per cent of our AGNs are classified as Seyfert galaxies and two (VV 705 and ESO186–IG019) as low-ionization nuclear emission-line regions (LINERs). One of our sources (PKS 1549–79) is a quasar (see Netzer 2015 for a review on AGN classification), while PKS 1549-79, 3C 84 (Perseus A, NGC 1275), 3C 405 (Cygnus A), and 3C 433 are also known as radio sources.

The 8–1000 μm infrared luminosities L_{IR} (from Sanders et al. 2003) cover the range $10^{10}L_\odot < L_{IR} < 10^{12.5}L_\odot$. The bulk (43 per cent) of our sample is made of luminous infrared galaxies (LIRGs, $10^{11} \leq L_{IR}/L_\odot < 10^{12}$), while ultra-luminous infrared galaxies (ULIRGs, $L_{IR} \geq 10^{12}L_\odot$) account for 27 per cent of the sample; the remaining 30 per cent have $10^{10} < L_{IR} < 10^{11}L_\odot$. It is thought that the (U)LIRG phenomenon is mainly linked to merger activity (Lonsdale, Farrah & Smith 2006), especially for $L_{IR} \geq 10^{11.5}$ $L_\odot$ (Hung et al. 2014; Pérez-Torres et al. 2021), as during mergers the gas can reach very high gas densities, triggering intense SF (Larson & Tinsley 1978). Mergers and interactions can also trigger AGN activity for the very same reason: the gas has the opportunity to lose its angular momentum and fall from kpc-scale distances to the inner parsecs from the nucleus (Alonso-Herrero et al. 2012; Treister et al. 2012; Ricci et al. 2017b; Ellison et al. 2019). Both SF and AGN phenomena heat the dust, hence boosting the IR luminosity of the host galaxies. Within our sample, at least five galaxies show an evolved merging phase: ESO 148-IG002 (Leslie et al. 2014), IRAS 19254-7245 (Superantennae, Bendo, Clements & Khan 2009), NGC 6240 (Komossa et al. 2003), Mrk 463 (Bianchi et al. 2008) and VV 705 (Perna et al. 2019). Seven more galaxies have a very close companion: NGC 3227 (∼15 kpc, Mundell et al. 2004), NGC 7465 (∼15 kpc, Merkulova et al. 2012), NGC 7469 (∼20 kpc, Zaragoza-Cardiel et al. 2017), NGC 7674 (∼20 kpc, Larson et al. 2016), MCG+04-48-002 (∼25 kpc, Koss et al. 2016), TOL1238-364 (∼25 kpc, Temporin et al. 2003), and IC4518a (∼1 kpc, Bellocchi, Arribas & Colina 2016). Two additional sources (NGC 34 and ESO 286-IG019) have a disturbed morphology, sign of a past galactic interaction. Moreover, some of the galaxies of this sample (notably NGC 5128, 3C 84, and 3C 405) are known to be part of groups or clusters, so their morphology is unsettled by probable continuous interactions with nearby satellite galaxies. Same as for the (U)LIRGs, interacting galaxies and systems with disturbed morphologies are typically characterized by higher molecular gas content and star formation activity than isolated galaxies that may be due to tidal torques able to produce gas infall from the surrounding regions (e.g. Combes et al. 1994; Casasola, Bettoni & Galletta 2004; Pan et al. 2018; Moreno et al. 2019).

3 DATA COLLECTION

3.1 X-ray data

We collect the best X-ray data available for our sample, namely the intrinsic 2–10 keV luminosity (L_X), the column density (N_H) of the obscuring material, and the photon index Γ (Reynolds 1997; Osterbrock & Ferland 2006; Singh, Shastri & Risaliti 2011) of the X-ray spectrum. To minimize both the contribution from host galaxy X-ray emission processes such as X-ray binaries, and the obscuration of the AGN (Hickox & Alexander 2018), we prioritize hard-X *NuSTAR* (3–78 keV, Harrison et al. 2013) and *Swift/BAT* (15–150 keV, Gehrels et al. 2004; Barthelmy et al. 2005; Krimm et al. 2013) observations.

Table 1. Properties of the sample of 35 AGN.

Name	RA (deg)	Dec. (deg)	D_L (Mpc)	D_{25} (arcsec)	Class	logL_X (erg s^{-1})	logN_H (cm^{-2})	log L_{IR} (L$_\odot$)	log M_{mol} (M$_\odot$)	SFR (M$_\odot$ yr^{-1})	Sample
NGC 0034	2.78	−12.11	85	69	S2	42.11	23.72	11.44	9.97	31	klr-sn
UGC 00545	13.40	12.69	264	29	Q	43.60	–	11.95[d]	10.17	34	k-n
NGC 1068	40.67	−0.01	16	370	S1h	42.38	24.70	11.27	10.14	17	klmr-cbn
3C 84	49.95	41.51	76	128	S1.5	43.98	21.68	11.20	9.63	9.0	kl-b
NGC 1365	53.40	−36.14	23	721	S1.8	42.32	22.21	11.00	10.10	17	kr-bn
IRAS F05189-2524	80.26	−25.36	188	30	S1h	43.20	22.86	12.11	10.04	109	klpr-sbn
IRAS 07598+6508	121.14	65.00	704	39[c]	S1	42.10	–	12.46[e]	10.54	–	kp-n
UGC 05101	143.97	61.35	174	72	S1	43.08	24.08	11.95	10.21	105	klp-xbn
NGC 3227	155.88	19.87	17	239	S	42.10	20.95	10.13	9.02	0.56	k-bn
NGC 4151	182.64	39.41	14	173	S	42.31	22.71	10.20	7.42	0.25	k-bn
NGC 4388	186.45	12.66	36	322	S1h	42.60	23.50	10.00	9.40	3.7	k-sbn
TOL 1238-364	190.22	−36.76	47	76	S1h	43.40	24.95	10.62	8.94	4.1	k-s
Mrk 0231	194.06	56.87	186	85	S1	42.50	22.85	12.51	10.39	278	klpmr-n
MCG -03-34-064	200.60	−16.73	72	81	S1h	43.18	23.80	11.24	–	5.7	kl-sbn
NGC 5128	201.37	−43.02	8	1542	S2[h]	42.39	23.02	10.11	10.17	6.7	k-b
NGC 5135	201.43	−29.83	59	144	S2	41.97	24.47	11.17	10.17	17	rlk-s
Mrk 0463	209.01	18.37	224	64	S1h	43.28	23.83	11.77[e]	9.92	–	kp-sbn
IC 4518a	224.42	−43.13	71	55	S2	42.64	23.36	11.13	–	5.6	kl-b
VV 705[a]	229.53	42.75	177	39	S2[h]	42.30	23.93	11.89	10.37	72	kl-n
PKS 1549−79	239.25	−79.24	725	–	S1[h]	44.71	20.00	12.36[d]	10.01[g]	–	k-b
PG 1613+658	243.49	65.72	605	27	Q	44.19	20.00	12.00	10.24	44	k-b
NGC 6240	253.25	2.40	107	131	S3	43.58	24.20	11.85	10.58	70	klpmr-cbn
IRAS 19254–7245[b]	292.84	−72.66	277	38	S2[h]	42.80	23.58	12.06[e]	10.34	104	kp-n
3C 405	299.87	40.73	250	33	S1.9	44.37	23.38	<11.75[f]	<8.88	35	k-b
MCG +04-48-002	307.15	25.73	60	60	S2[h]	43.13	23.86	11.06	9.64	10	kl-b
IC 5063	313.01	−57.07	49	161	S1h	42.87	23.42	10.85	9.36	2.6	k-sb
ESO 286-IG019	314.61	−42.65	190	41	H2	42.30	23.69	12.00	10.25	105	klp-n
3C 433	320.94	25.07	468	19	S2	44.16	23.01	<11.66[f]	<9.71	10	k-b
NGC 7130	327.08	−34.95	70	93	S1.9	42.30	24.10	11.35	10.10	22	kl-scb
NGC 7172	330.51	−31.87	37	151	S2	42.76	22.91	10.45	9.58	2.5	k-bn
NGC 7465	345.50	15.97	28	64	S3	41.97	21.46	10.10	8.88	0.76	k-b
NGC 7469	345.82	8.87	71	83	S	43.19	20.53	11.59	10.09	35	klr-bn
ESO 148-IG002	348.95	−59.05	198	56	H2	43.20	–	12.00	10.05	108	klp-n
NGC 7582	349.60	−42.37	23	415	S1i	42.53	24.20	10.87	9.64	7.1	k-cbn
NGC 7674	351.99	8.78	127	67	S1h	43.60	–	11.50	10.46	15	kl-n

Notes. RA, Dec. from NED. D_L is the luminosity distance, calculated from the redshift (taken from NED) according to the adopted cosmology. D_{25} is the optical diameter, measured at the isophotal level 25 mag arcsec^{-2} in the *B* band, taken from HyperLEDA. Class is the AGN classification from HyperLEDA: *Q* = quasar, *S*1 = broad-line Seyfert 1, S1i = S1 with a broad Paschen H β line, S1h = S2 that show S1-like spectra in polarized light, S2 = Seyfert 2, S1.5 = Seyfert 1.5, S1.8 = Seyfert 1.8, S1.9 = Seyfert 1.9, S = AGN objects without classification, S3 = LINERs, H2 = extragalactic H II regions. L_X is the 2–10 keV intrinsic (i.e. corrected for source absorption) luminosity, taken from the works indicated in the Sample column (see Section 3.1 for details). L_{IR} is the 8–1000 μm luminosity, from Sanders et al. (2003) unless otherwise specified. M_{mol} is the total molecular mass, calculated as described in Section 3.5. SFR is the star formation rate, calculated as described in Section 5.1. Sample lists the references for the CO *Herschel* fluxes [*r* for Rosenberg et al. (2015), *m* for Mashian et al. (2015), *p* for Pearson et al. (2016), *k* for Kamenetzky et al. (2016), *l* for Lu et al. (2017)] and for the X-ray data [*n* for Brightman & Nandra (2011), *b* for Ricci et al. (2017a), *c* for Marchesi et al. (2019), *x* for La Caria et al. (2019), *s* for Salvestrini et al. (in preparation)].
[a]RA, Dec. from Kojoian, Elliott & Tovmassian (1981). [b]RA, Dec. from Westmoquette et al. (2012). [c]D_{25} from NED. [d]L_{IR} from Moshir et al. (1990). [e]L_{IR} from Pearson et al. (2016). [f]Upper limit for L_{IR} from Golombek, Miley & Neugebauer (1988). [g]M_{H_2} from Oosterloo et al. (2019). [h]Class from NED.

The data are taken from Ricci et al. (2017a), Marchesi et al. (2019), La Caria et al. (2019), and Salvestrini et al. (in preparation). When not available in these works, we take the L_X and N_H derived from *XMM–Newton* in the 0.5–10 keV band by Brightman & Nandra (2011). In Table 1, we list the data together with their references. The final sample has a median[2] log L_X [erg s^{-1}] = $42.8^{+0.8}_{-0.5}$.

L_X is the intrinsic (i.e. unobscured) luminosity of the AGN, after taking into account the obscuration of the gas along the line of sight. Obscuration of AGN radiation is usually measured in terms of column density (N_H), and it originates from the immediate vicinity of the accretion disc, in the form of a compact (∼0.1–10 pc) dusty torus (Ramos Almeida & Ricci 2017). However, as pointed out by recent works (e.g. Buchner & Bauer 2017; D'Amato et al. 2020), the obscuring gas can also be associated with the host galaxy on larger (∼10 pc–1 kpc) scales. For our sample, the median N_H is log(N_H/cm^{-2}) = $23.5^{+0.7}_{-1.8}$, with 27 of them being type 2 AGN (i.e. they have $N_H > 10^{22}$ cm^{-2}, Hickox & Alexander 2018), and six Compton-thick AGN ($N_H \geq 1.5 \times 10^{24}$ cm^{-2}, Matt et al. 2000; Comastri 2004). Assuming that this gas is distributed over a sphere of 250 pc radius,[3] the average gas density is log(n/cm^{-3}) = $2.6^{+0.7}_{-1.7}$.

[2]The errors on the medians presented in this paper always refer to the 16th and the 84th percentile of the data distribution.

[3]See Section 3.3 for a definition of this radius

3.2 Herschel CO data

In the local Universe, the mid-*J* and high-*J* CO transitions have been observed with the *Herschel* Space Observatory (Pilbratt et al. 2010). In particular, the transitions from CO(4–3) (CO(5–4) for galaxies with $D_{\rm L} > 150$ Mpc) to CO(13–12) have been observed with the Spectral and Photometric Imaging Receiver (SPIRE) Fourier Transform Spectrometer (FTS) instrument (Griffin et al. 2010) aboard *Herschel*. The beam full width at half-maximum (FWHM) of the SPIRE-FTS *Herschel* observations (Lu et al. 2017) ranges from 16.6 arcsec at 200 μm to 42.8 arcsec at 650 μm, respectively, corresponding to the rest-frame wavelengths of CO(13–12) and CO(4–3). The beam FWHMs correspond to physical scales in the range ∼6–14 kpc at the median redshift $z = 0.02$ of our sample.

We collect SPIRE data from Rosenberg et al. (2015), Mashian et al. (2015), Pearson et al. (2016), Kamenetzky et al. (2016), and Lu et al. (2017), which altogether account for CO fluxes from 226 galaxies. In Table 2, we report the CO fluxes used in this work and, in case of multiple observations, we adopt the mean and the standard deviation of the observed fluxes as fiducial values.

3.3 ALMA ancillary data

In local ($D \sim 1$ Mpc) sources, the Atacama Large Millimeter Array (ALMA) is able to resolve the morphology of CO emission at ∼100 pc scales, from CO(1–0) to the mid-*J* CO(6–5) line. Higher-*J* lines, which trace the dense/warm molecular gas possibly influenced by the X-ray photons, fall unfortunately out of the ALMA bands at low redshift. From the ALMA archive,[4] we therefore collect all the available maps of the highest possible CO transition – namely the CO(6–5) – for the galaxies in our sample. We use these maps to infer the size of the high-density molecular gas region that cannot be estimated from the *Herschel* data given their poor spatial resolution. As the critical density of the CO transitions increases with *J* ($n_{\rm crit} \propto (J+1)^3$), and given that the gas density increases as we get closer to the galaxy centre, we expect the higher-*J* lines to originate from an area extended at most like CO(6–5) (see e.g. Mingozzi et al. 2018). We thus use the typical size of the CO(6–5) emitting region as an upper limit for the AGN sphere of influence on the molecular gas.

Fig. 1 shows – as an illustrative example – the spatially resolved CO(6–5) emission from NGC 34, a LIRG in our sample, hosting an obscured ($N_{\rm H} = 10^{23.7}$ cm^{-2}) AGN (Brightman & Nandra 2011; Mingozzi et al. 2018). For this source, we retrieved two different ALMA observations, 2011.0.00182.S (PI: Xu) and 2016.1.01223.S (PI: Baba), both carried out in band 9, where the field of view (FoV) is ∼ 8.6 arcsec, but with different spatial resolutions (200 and 35 mas, respectively) and maximum recoverable scales (2 and 0.5 arcsec, respectively). These scales correspond to 800 and 200 pc at the NGC 34 distance. The total flux of the CO(6–5) detection with a resolution of 200 mas is $S_{\rm CO(6-5)} = 707 \pm 106$ Jy km s^{-1}, obtained by Mingozzi et al. (2018), using CASA 4.5.2 (McMullin et al. 2007) and a natural weighting scheme. This flux, which is shown with the green contours in Fig. 1 (see also Xu et al. 2014; Mingozzi et al. 2018), matches that recovered by *Herschel*/SPIRE within a much larger beam of 31.2 arcsec. This means that this ALMA observation, despite having a smaller FoV with respect to that of SPIRE, recovers all the CO(6–5) emission from the galaxy.

The high-resolution data (project ID 2016.1.01223.S, PI: Baba) are plotted with black contours in Fig. 1 and have never been published so far. We used the already calibrated and cleaned data cube from the ALMA Archive. For this data cube, calibration and imaging have been done manually, with a Briggs weighting (robust parameter of 0.5), and passed the QA2 stage. Using CASA 5.6 (McMullin et al. 2007), we produced the moment 0 map from the data cube with the task `immoments`. To estimate the flux, we performed a 2D Gaussian fit with the task `imfit`, which returned 62 ± 3 Jy km s^{-1}, less than 10 per cent of the total flux measured by SPIRE-FTS (920 ± 56 Jy km s^{-1}). The reason for this discrepancy is that this observation is limited by a much smaller maximum recoverable scale, compared to the 200-mas data. The emission consists of a single clump of $r \lesssim 50$ pc.

In addition to NGC 34, we analysed ALMA CO(6–5) maps available for NGC 1068 (García-Burillo et al. 2014), IRAS F05189–2524 (still unpublished), NGC 5128 (Espada et al. 2017), NGC 5135 (Sabatini et al. 2018), NGC 6240 (still unpublished), and NGC 7130 (Zhao et al. 2016). The images (Figs B1–B6) are shown in Appendix B. All these sources are characterized by spatially resolved CO(6–5) emission arising from the galaxy centre and extending up to 150–1000 pc, with median $r = 250$ pc. We therefore assume that the bulk of higher *J* CO line luminosity – for which we have only *Herschel* at low resolution – arise from a comparable region of radius $r = 250$ pc. In what follows, we use this size as an upper limit for $J \geq 6$ transitions emitting region.

3.4 Dust continuum emission as a proxy for star formation

Dust in active galaxies can be heated by both the UV/optical photons coming from black hole accretion, and UV/optical photons associated with star formation processes (e.g. Hatziminaoglou et al. 2008; Pozzi et al. 2010; Gruppioni et al. 2016). In the first case, the dust is mostly circumnuclear, which means it occupies the central 100 pc at most (e.g. Hickox & Alexander 2018); in the second case the dust grains reside in the star-forming regions through the galaxy structure. The emission of two dust components peaks at different infrared (IR) wavelengths, due to the different temperatures: the circumnuclear dust ($T \approx$ 60–100 K) peaks in the mid-IR, around 10–30 μm (Alonso-Herrero et al. 2011; Feltre et al. 2012), while the galactic diffuse dust is colder ($T \approx$ 20–30 K), peaking in the far-IR around 70 ∼ 100 μm (da Cunha, Charlot & Elbaz 2008).

For this reason, we adopt the 70 μm emission maps from the *Herschel* Photoconductor Array Camera and Spectrometer (PACS; Poglitsch et al. 2010) as a proxy for SF in our sample galaxies. In this regime, the AGN contamination, if any, accounts for a few per cent, and the spatial resolution at 70 μm (FWHM = 5.6 arcsec, corresponding to ∼0.17–13 kpc for our sample) is better than at longer wavelengths. We find suitable maps for all the sources, except IRAS 07598+6508, Mrk 463 and PKS 1549−79. We keep anyway these three galaxies in our sample for completeness.

The 5.6 arcsec spatial resolution allows us to map the distribution of SF, assuming that all the 70 μm photons trace the original stellar UV radiation. From visual inspection, SF is occurring mostly in the central regions ($r \sim 2$ kpc) of our galaxies. The procedure to extract the star formation rate (SFR) and the radial profile of the Habing field from the 70 μm data is outlined in Section 5.1.

3.5 Low-J CO data

To complete the CO SLEDs observations from *Herschel* discussed in Section 3.2, we collect (see Table 2) the low-*J* fluxes available in the literature, from CO(1–0) to CO(3–2). These

[4] https://almascience.eso.org/asax/

Table 2. CO SLED transitions in units of log ($L/L_\odot$).

CO transition Name	1–0	2–1	3–2	4–3	5–4	6–5	7–6	8–7	9–8	10–9	11–10	12–11	13–12
NGC 0034	5.22	5.83	–	<6.26	6.57	6.67	6.72	6.75	6.72	6.57	6.63	6.48	6.37
UGC00545	5.42[a]	6.25[a]	6.92[a]	–	–	<7.08	<7.01	<7.15	7.22	<7.14	<7.18	<7.04	<7.17
NGC 1068	5.39[b]	5.62[b]	6.20[a]	6.28	6.27	6.28	6.24	6.24	6.17	6.15	6.12	6.08	5.83
3C 84	4.85[c]	4.48[d]	5.92[e]	<6.48	6.39	6.32	6.25	6.33	6.41	6.45	6.32	6.31	6.13
NGC 1365	5.35	5.50	5.96	6.53	6.60	6.58	6.54	6.48	6.30	6.14	6.08	5.86	<5.77
IRASF05189-2524	5.28[a]	6.02[a]	6.49[a]	<7.04[a]	7.06	7.11	7.14	7.22	7.04	7.23	7.15	7.09	7.06
IRAS07598+6508	5.78[f]	6.57[f]	–	–	<8.08	<7.70	<7.77	<7.62	–	<8.06	<8.00	<8.05	<8.02
UGC05101	5.38[a]	6.37[a]	6.78[a]	–	7.00	7.10	6.95	7.02	6.89	7.05	6.87	6.36	6.69
NGC 3227	4.15[g]	4.82[h]	5.23[h]	5.41	5.48	5.44	5.30	5.34	5.19	5.11	5.24	5.15	<5.25
NGC 4151	2.55[i]	3.23[j]	–	<5.14	–	<4.84	4.66	<5.02	<5.14	5.26	<5.24	<5.18	5.03
NGC 4388	4.40[h]	5.15[h]	5.16[h]	6.05	5.91	5.94	5.84	5.83	5.78	5.71	<5.96	<5.93	<5.90
TOL1238-364	4.18[k]	5.15[k]	–	<5.92[k]	5.79	5.49	5.30	5.58	5.90	<5.98	<6.06	<5.90	<6.16
Mrk0231	5.54[a]	6.39[a]	6.83[a]	7.25[a]	7.28	7.33	7.41	7.44	7.35	7.45	7.36	7.29	7.23
MCG-03-34-064	–	–	–	<6.22	<6.20	5.97	5.96	<6.25	<6.31	6.38	6.05	6.09	6.14
NGC 5128	4.85[l]	4.57[m]	4.90[m]	4.51	4.57	4.48	4.32	4.29	<4.48	<4.27	<4.19	<4.24	<4.62
NGC 5135	5.19[a]	6.00[a]	6.38[a]	6.51	6.61	6.61	6.49	6.37	6.31	6.13	6.03	5.95	5.65
Mrk0463	5.12[n]	5.08[o]	–	–	<7.05	6.81	6.67	6.61	<7.03	6.37	<7.05	<7.08	–
IC4518a	–	–	–	6.66	6.28	6.24	5.99	6.14	<6.29	<6.16	6.25	<6.07	<6.28
VV705	5.61[a]	5.78[p]	6.59[a]	–	7.04	6.83	6.95	6.89	<7.04	6.77	6.79	6.79	6.70
PKS1549-79	–	–	–	–	<8.26	<7.95	<7.71	–	–	<7.92	<7.81	<7.98	<7.99
PG1613+658	5.49[f]	–	–	–	<7.99	<8.00	–	<7.59	–	<7.83	–	<7.94	<7.87
NGC 6240	5.63[a]	6.59[a]	7.10[a]	7.46	7.59	7.69	7.75	7.78	7.75	7.72	7.65	7.59	7.52
IRAS19254-7245	5.59[n]	–	–	–	–	7.01	7.31	7.20	7.32	7.21	7.04	6.85	7.07
3C 405	<4.12[c]	–	–	–	<7.21	<7.01	<6.85	–	<7.21	–	<7.06	–	<7.13
MCG+04-48-002	4.88[q]	–	–	<6.61	6.32	6.11	6.13	6.18	<6.25	<6.33	<6.33	<6.18	<6.34
IC5063	4.51[h]	–	–	–	<6.17	<5.88	5.77	<6.00	<6.10	<6.15	–	<6.12	<6.17
ESO286-IG019	5.50[r]	–	6.30[s]	–	7.22	7.13	7.30	7.36	7.22	7.37	7.33	7.25	7.18
3C 433	<4.96[c]	–	–	–	<7.76	<7.63	<7.38	<7.40	–	<7.37	<7.54	<7.55	–
NGC 7130	5.34[q]	5.72[p]	–	6.70	6.71	6.66	6.62	6.51	6.58	6.43	6.34	6.18	6.11
NGC 7172	4.75[p]	5.25[t]	–	<6.10	<5.79	5.64	<5.41	<5.62	<5.59	–	<5.67	–	<5.77
NGC 7465	4.13[g]	4.52[u]	4.92[e]	<5.59	5.38	<5.35	<5.24	<5.61	<5.66	<5.64	<5.42	–	–
NGC 7469	5.24[a]	6.02[a]	6.44[a]	6.69	6.83	6.80	6.71	6.62	6.58	6.40	6.35	6.20	6.15
ESO148-IG002	5.29[n]	–	–	–	6.99	7.04	7.15	7.13	7.14	7.09	7.02	6.89	7.03
NGC 7582	4.57[h]	5.53[t]	–	5.95	6.03	6.04	5.94	5.87	5.83	5.66	5.51	<5.41	<5.64
NGC 7674	5.70[v]	5.93[h]	6.26[h]	<6.95	<6.57	6.32	6.09	6.36	<6.68	<6.59	<6.63	6.59	<6.64

Notes. All the CO line luminosities are taken from Rosenberg et al. (2015), Mashian et al. (2015), Pearson et al. (2016), Kamenetzky et al. (2016), Lu et al. (2017) unless otherwise specified. [a]Data from Papadopoulos et al. (2012): CO(1–0) was observed with IRAM-30m (FWHM: 22 arcsec), CO(2–1) (FWHM: 20 arcsec), CO(3–2) (FWHM: 14 arcsec) and CO(4–3) (FWHM: 11 arcsec) with JCMT. [b]Data from Curran et al. (2001); [c]Data from Evans et al. (2005): 3C 84 and 3C 433 were observed with NRAO-12m (FWHM: 55 arcsec), 3C 405 was observed with IRAM-30m (FWHM: 22 arcsec). [d]Data from Salomé et al. (2011), observed with IRAM-30m (FWHM: 11 arcsec). [e]Data from Mao et al. (2010), observed with HHT (FWHM: 22 arcsec). [f]Data from Xia et al. (2012): CO(1–0) (FWHM: 22 arcsec) and CO(2–1) (FWHM: 11 arcsec) were observed with IRAM-30m. [g]Data from Maiolino et al. (1997), observed with NRAO-12m (FWHM: 55 arcsec). [h]Data from Israel (2020); [i]Data from Dumas, Schinnerer & Mundell (2010); [j]Data from Rigopoulou et al. (1997), observed with JCMT (FWHM: 20 arcsec). [k]Data from Pereira-Santaella et al. (2013); [l] Data from Espada et al. (2019); [m]Data from Israel (1992), observed with SEST (FWHM: 23 arcsec), CO(3–2) was observed with CSO (FWHM: 20 arcsec). [n]Data from Gao & Solomon (1999): ESO148-IG002 and IRAS19254-7245 were observed with SEST (FWHM: 44 arcsec), Mrk0463 was observed with IRAM-30m (FWHM: 24 arcsec). [o]Data from Alloin et al. (1992), observed with IRAM-30m (FWHM: 13 arcsec). [p]Data from Albrecht, Krügel & Chini (2007); [q]Data from Gao & Solomon (2004); [r]Data from Ueda et al. (2014); [s]Data from Imanishi, Nakanishi & Izumi (2017); [t]Data from Rosario et al. (2018); [u]Data from Monje, Blain & Phillips (2011); [v]Data from Young et al. (1995).

transitions have been observed using several single-dish telescopes: the 14-m Five College Radio Astronomy Observatory (FCRAO), the 15-m Swedish-ESO Submillimeter Telescope (SEST), the 30-m Institut de Radioastronomie Millimétrique Pico Veleta telescope (IRAM-30m), the 12-m Atacama Pathfinder Experiment (APEX), and the 15-m James Clerk Maxwell Telescope (JCMT).

We expect these low-J CO lines to trace a larger area than mid-J and high-J lines, since they are characterized by lower $n_{\rm crit}$ and lower excitation temperatures. CO(1–0) is especially important since its flux is the most widely used proxy for the total molecular gas mass of a galaxy (Bolatto et al. 2013). For the closest galaxies, their projection on the sky could result larger than the telescope collecting area. For this reason, when multiple observations are available, we prioritize mosaics and larger beams.

Many authors have found that CO(1–0) emitting gas has an exponential radial profile, and that there is a relation between the CO(1–0) scale length $r_{\rm CO}$ and the optical radius r_{25} (Leroy et al. 2008; Schruba et al. 2011; Villanueva et al. 2021). Since the $\sim$30 per cent of our sample contains highly inclined galaxies ($i \geq 60^\circ$), we follow Boselli, Cortese & Boquien (2014) and Casasola et al. (2020) assuming that the CO(1–0) emission is well described by an exponential decline both along the radius r and above the galactic plane on the z-direction (3D method):

$$S_{\rm CO}(r, z) = S_{\rm CO,tot} e^{-r/r_{\rm CO}} e^{-|z|/z_{\rm CO}}, \quad (1)$$

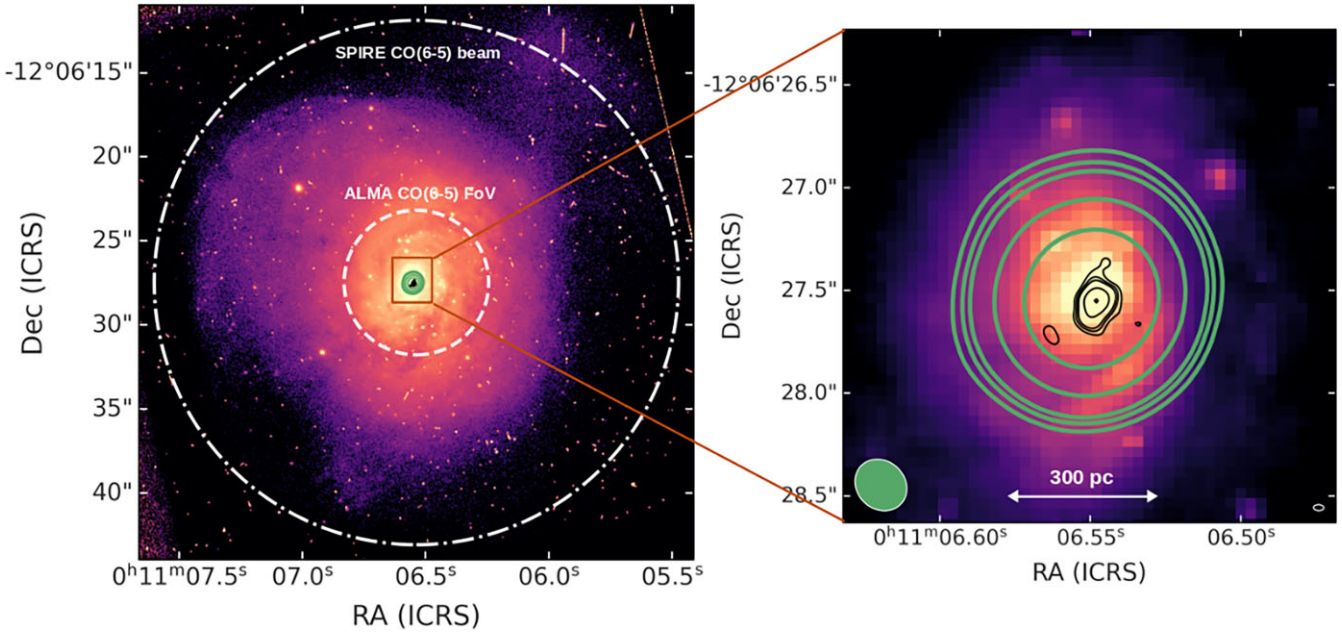

Figure 1. *Left-hand panel: HST* WFPC2 F606W image of NGC 34 (from Malkan, Gorjian & Tam 1998) with superimposed the contours of two ALMA CO(6–5) observations, in green at the resolution of 200 mas, in black of 35 mas. Both the contours are at the respective (3, 4, 5, 10, 20) $\times\,\sigma$, where σ = 3.1 Jy beam^{-1} km s^{-1} for the green lines and σ = 0.27 Jy beam^{-1} km s^{-1} for the black lines. The inner white dashed circle indicates the FoV of both ALMA observations, with a radius of 4.3 arcsec ($\sim$1.7 kpc), while the outer dash–dotted circle represents the *Herschel*/SPIRE-FTS beam FWHM for CO(6–5) observations, with a 15.6 arcsec radius. *Right-hand panel:* zoom of the inner 1 kpc. Restored ALMA beams of the 200 and 35 mas images are shown as ellipses with white edges, at the bottom left (with the green area) and right (with the black area), respectively. The 35 mas ALMA image has not been primary-beam corrected.

where $r_{\rm CO} = 0.17\,r_{25}$ and $z_{\rm CO} = 0.01\,r_{25}$, as in Casasola et al. (2017) and Boselli et al. (2014). We stress that for galaxies with low inclination, the 3D method is analogous to the standard 2D approach, such as that developed by Lisenfeld et al. (2011). The adopted approach provides a median $r_{\rm CO} = 3.07^{+2.06}_{-1.48}$ kpc for our sample.

4 CO EMISSION ON GLOBAL GALACTIC SCALES

Before investigating the PDR versus XDR contribution to the molecular gas heating in the center of our sample galaxies, we want to see if, on the scale of the whole galaxy, it is already possible to see the influence of the AGN on the molecular gas phase. We check how our active galaxies compare to other active and non-active samples on the Schmidt–Kennicutt plane (Schmidt 1959; Kennicutt 1998), which links the molecular gas surface density $\Sigma_{\rm mol}$ and the SFR surface density $\Sigma_{\rm SFR}$, i.e. the star formation to its fuel.

We calculate the surface densities $\Sigma_{\rm mol}$ and $\Sigma_{\rm SFR}$ within the CO radius $r_{\rm CO}$, defined as a fraction of the optical radius r_{25} (see Section 3.5). We derive the molecular mass from the CO(1–0) flux in the following way. For each source, we have the CO(1–0) flux $S_{\rm CO}$, measured within the telescope beam, with FWHM 2θ, in angular units (the factor of 2 is due to the fact that the FWHM is a diameter, while we want a radius). In spatial units (e.g. in pc) in the source reference frame, this corresponds to a radius r_θ, so that the flux recovered by the telescope is

$$S_{\rm CO}(r_\theta) = \int\!\!\int_0^{r_\theta} S_{\rm CO}{\rm d}r{\rm d}z = S_{\rm CO,tot}({\rm e}^{-r_\theta/r_{\rm CO}} - 1)({\rm e}^{-r_\theta/z_{\rm CO}} - 1). \quad (2)$$

If we put $r_{\rm CO}$ instead of r_θ in equation (2), we obtain that $S_{\rm CO}(r_{\rm CO}) \approx 0.63 S_{\rm CO,\,tot}$. Given that we know $S_{\rm CO}(r_\theta)$ from observations, we can calculate the CO(1–0) flux within $r_{\rm CO}$:

$$S_{\rm CO}(r_{\rm CO}) = \int\!\!\int_0^{r_{\rm CO}} S_{\rm CO}(r,z){\rm d}r{\rm d}z = \frac{0.63\,S_{\rm CO}(r_\theta)}{({\rm e}^{-r_\theta/r_{\rm CO}} - 1)({\rm e}^{-r_\theta/z_{\rm CO}} - 1)}. \quad (3)$$

We find a median ratio $S_{\rm CO}(r_{\rm CO})/S_{\rm CO}(r_\theta) = 0.70^{+0.30}_{-0.06}$, with only one galaxy (NGC 5128) having $S_{\rm CO}(r_{\rm CO})/S_{\rm CO}(r_\theta) > 2$. From the CO(1–0) flux calculated within $r_{\rm CO}$, we estimate the molecular mass by using the following equation from Bolatto et al. (2013):

$$M_{\rm mol} = 1.05 \times 10^{-16} X_{\rm CO} \frac{S_{\rm CO} D_{\rm L}^2}{1+z}\,{\rm M}_\odot\,, \quad (4)$$

where $S_{\rm CO}$ is the CO(1–0) flux in Jy km s^{-1}, $D_{\rm L}$ is the luminosity distance in Mpc, z is the redshift, and $X_{\rm CO}$ is the CO-to-H_2 conversion factor. The masses thus calculated already take into account the contribution of helium and heavy elements. To line up with the other samples included in our comparison, we adopt a Milky Way value of $X_{\rm CO} = 2 \times 10^{20}$ cm^{-2} (K km s^{-1})$^{-1}$, corresponding to $\alpha_{\rm CO} = 4.3$ M$_\odot$ (K km s^{-1} pc^{-2})$^{-1}$, defined as the mass-to-light ratio between $M_{\rm mol}$ and the CO(1–0) luminosity.

We find $M_{\rm mol}$ between $10^{7.4}$ and $10^{10.6}$ M$_\odot$, with median $\log(M_{\rm mol}/{\rm M}_\odot) = 10.1^{+0.3}_{-0.7}$. These $M_{\rm mol}$ are calculated within $r_{\rm CO}$: to extrapolate the results to the whole galaxy ($r \to +\infty$), a multiplicative factor of 1/0.63 is needed. The molecular masses calculated using equations (3) and (4) are reported in Table 1, while the uncorrected (i.e. the observed) CO luminosities are the ones in Table 2. We note that these masses could be upper limits, since we are adopting a Milky Way value of $\alpha_{\rm CO}$, while it is thought that dusty (U)LIRGs and starburst galaxies have a lower $\alpha_{\rm CO} \approx 0.8$ M$_\odot$ (K km s^{-1} pc^{-2})$^{-1}$ (Downes & Solomon 1998; Bolatto et al. 2013).

The SFRs are estimated from the radial profile $F_{70}(r)$ of the 70 μm photometry maps: $\log {\rm SFR} = \log L_{70} - 43.23$ (Calzetti et al. 2010;

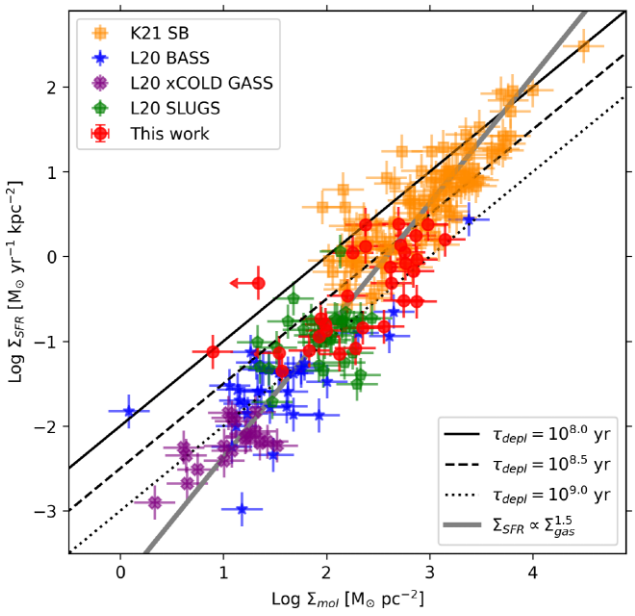

Figure 2. Schmidt–Kennicutt relation for our sample of active galaxies (red circles), the starburst sample from Kennicutt & De Los Reyes 2021 (orange squares), and the AGN sample (blue stars) and normal SFG (pink crosses and green pentagons) from L20. Lines of constant molecular gas depletion times are overlayed to the data. The grey solid line is the best fit for a single relation as reported by Kennicutt & De Los Reyes (2021), namely $\log \Sigma_{\rm SFR} = 1.5 \log \Sigma_{\rm mol} - 3.87$. All molecular surface densities were derived using the Milky Way value $\alpha_{\rm CO} = 4.3$ $M_\odot$ (K km s^{-1} pc^{-2})$^{-1}$.

Kennicutt & Evans 2012), where L_{70} is in units of erg s^{-1} and comes from the integration of $F_{70}(r)$ up to $r_{\rm CO}$. This SFR calibration depends on the quantity of dust (it works better for dusty starburst galaxies) and the stellar population mix, and works better for galaxies with $L_{70} > 4.4 \times 10^9$ $L_\odot$ (Calzetti et al. 2010), which is satisfied by the ~ 90 per cent of our galaxies. Using this SFR calibration, we find a median SFR $= 12.5^{+34.9}_{-9.8}$ $M_\odot$ yr^{-1}.

In Fig. 2, we show our galaxies in the $\Sigma_{\rm mol}$–$\Sigma_{\rm SFR}$ plane, comparing them with starburst (SB) galaxies from Kennicutt & De Los Reyes 2021 (K21, hereafter), AGN observed with Swift/BAT from the BASS sample (Ricci et al. 2017a), star-forming galaxies (SFG) from the xCOLD GASS survey (Saintonge et al. 2017), and IR luminous galaxies from SLUGS (Dunne et al. 2000). The latter three samples were gathered by Lamperti et al. 2020 (L20, hereafter).

Our estimates of $\Sigma_{\rm mol}$ and $\Sigma_{\rm SFR}$ mainly depend on the assumed CO exponential profile and the SFR–70 μm calibration. Following K21, we assign a conservative error of ±20 per cent to both $\Sigma_{\rm mol}$ and $\Sigma_{\rm SFR}$. Since we could not recover the data errors from every point of L20, we adopt the same ±20 per cent uncertainty also for their points.

We want to see if there is a difference between normal SFGs and AGN on the $\Sigma_{\rm mol}$–$\Sigma_{\rm SFR}$ plane. As shown in Fig. 2, our sample of AGN fit well in between the starburst galaxies of K21 and the mixed (AGN/SFGs) sources from L20. We note a gap between the K21 and L20 sources, probably due to the difference in the area assumed for deriving the surface densities: K21 calculate a circumnuclear starburst region differently for every galaxy, finding $r = 2.8^{+3.3}_{-1.2}$ kpc; L20 instead use the CO observation beam area, which has a FWHM of 15 arcsec for the SLUGS sample and 20 ∼ 22 arcsec for both the xCOLD GASS and the BASS sample (hence radii of 0.4 ∼ 11 kpc). Overall, we find that, on the kpc-scale, an AGN effect on the SF is not evident, thus confirming earlier findings from L20 and Koss et al. (2021), and from Casasola et al. (2015), who studied the Schmidt–Kennicutt relation for four AGN from the NUGA sample (García-Burillo et al. 2003).

In Fig. 2, we highlight the lines corresponding to constant depletion time, $\tau_{\rm depl} = \Sigma_{\rm mol}/\Sigma_{\rm SFR} = [10^8, 10^{8.5}, 10^9]$ yr, respectively. For the galaxies in our sample, we find a median $\log(\tau_{\rm depl}/{\rm yr}) = 8.9^{+0.4}_{-0.6}$, similar to other studies of Seyferts (e.g. Salvestrini et al. 2020), and slightly lower than typical values for local inactive SFGs (Bigiel et al. 2008; Utomo et al. 2018; Leroy et al. 2021, all find a median $\tau_{\rm depl} \sim 2 \times 10^9$ yr). Conversely, typical progenitors of ellipticals or proto-spheroids galaxy models (Calura et al. 2014) require $\tau_{\rm depl} \sim 2 \times 10^7$ yr, while dusty sub-millimetre galaxies (SMG), which are mostly hyperluminous infrared galaxies (HyLIRG, $L_{\rm IR} \geq 10^{13}$ $L_\odot$) at moderately high redshift ($z \sim 3$) can have even shorter $\tau_{\rm depl} \leq 10^7$ yr (Carilli & Walter 2013), but these are probably extreme and rare objects (Heckman & Best 2014).

From a classical evolutionary perspective, active, interacting (U)LIRGs are thought to be an intermediate stage between a late-type SFG and a quiescent early-type galaxy (Hopkins et al. 2008). From more recent works, it seems that interacting and merging systems can account only for the formation of the most massive ellipticals, while slow secular processes (in the local Universe) or rapid instabilities in clumpy gaseous disks (at high z) are responsible for the evolution of the bulk of the galaxies (Heckman & Best 2014). Within the limits of our analysis, we do not see a strong effect of AGN feedback on $\tau_{\rm depl}$ at kpc-scales, but that its impact also depends on the choice of $\alpha_{\rm CO}$.

5 CO EMISSION IN THE GALAXY CENTERS

We now focus on the CO emission in the inner 500 pc (i.e. up to $r = 250$ pc from the center) with the aim of assessing the relative contribution of PDR and/or XDR to the molecular gas in the vicinity of the AGN. To this goal, we exploit the line ratios with respect to CO(1–0) and CO(6–5): $L'_{\rm CO(J\rightarrow J-1)}/L'_{\rm CO(1-0}$ (i.e. high-J/low-J ratios) and $L'_{\rm CO(J\rightarrow J-1)}/L'_{\rm CO(6-5)}$ (i.e. high-J/mid-J ratios), where all $L'_{\rm CO}$ are in units of K km s^{-1} pc^{-2}. We use the CO(1–0) theoretical profile (equation 3) to calculate the flux within $r = 250$ pc:

$$S_{\rm CO}(r \leq 250\ {\rm pc}) = S_{\rm CO,tot}(e^{-250{\rm pc}/r_{\rm CO}} - 1)(e^{-250{\rm pc}/z_{\rm CO}} - 1). \quad (5)$$

Conversely, we do not correct the other CO lines: we know (Section 3.3) that CO(6–5) emission is mostly confined within the central 250 pc, and the same should likely apply for higher-J lines. There are few studies that map the size of other low-J lines than CO(1–0): Casasola et al. (2015) compares CO(1–0), CO(2–1), and CO(3–2) images for four nearby active galaxies (none of which is part of this sample), finding a similar physical size for the first two transitions and a halved size (mean ∼500 pc) for the available CO(3–2) maps; NGC 1068, however, has a CO(3–2) emission which extends beyond the central 2 kpc (García-Burillo et al. 2014). Among our sample of galaxies, Dasyra et al. (2016) have published a CO(4–3) image of IC 5063, which has a similar size (∼1 kpc) of its CO(2–1) emission. CO(4–3) images of IRAS F05189–2524, NGC 5135, ESO 286–IG019, NGC 7130, NGC 7469, and ESO 148–IG002, among other (U)LIRGs, are published by Michiyama et al. (2021), who find emitting sizes for the aforementioned galaxies between 1 and 5 kpc. Since these low-J CO transitions are not the focus of this work, and since we do not have a theoretical radial profile to correct them, we leave them unaltered, and put the relative plots only in the Appendix A (Figs A1–A4).

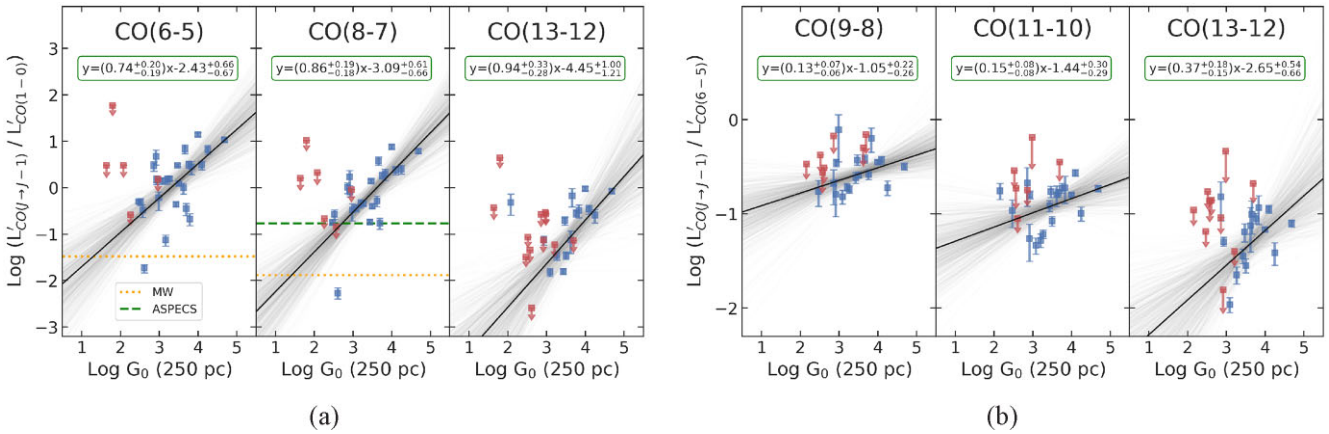

Figure 3. CO line ratios as a function of the Habing field, G_0, measured at $r = 250$ pc (see Section 5.1). We consider both the luminosity ratios $L'_{CO(J\rightarrow J-1)}/L'_{CO(1\rightarrow 0)}$ with respect to the CO(1–0) (left-hand panel, 3a) and $L'_{CO(J\rightarrow J-1)}/L'_{CO(6\rightarrow 5)}$ with respect to the CO(6–5) line luminosity (right-hand panel, 3b). The luminosities L' are in units of K km s^{-1} pc^{-2}, and J is indicated on the top of each panel. Blue squares indicate 3σ detections, while red squares with downward arrow indicate $<3\sigma$ detections in the higher-J line (i.e. censored data). The solid black line is the regression fit, with the underlying grey lines showing the fits drawn from the posterior distribution. When available, the Milky Way (dotted orange line, data from Fixsen, Bennett & Mather 1999) and the ASPECS AGN (green dashed line, data from Boogaard et al. 2020) CO ratios are also shown.

In the next two subsections, we derive the fluxes of FUV and X-ray photons, which are the heating drivers in PDRs and XDRs, respectively, and we compare them with the CO line ratios.

5.1 PDR

The FUV flux (also often referred to as interstellar radiation field) is measured in Habing units G_0, where $G_0 = 1$ corresponds to its value in the solar neighbourhood: 1.6×10^{-3} erg cm^{-2} s^{-1} in the FUV band (Habing 1968). As discussed in Section 3.4, the FUV photons are efficiently absorbed by dust grains, which re-emit energy in the infrared (IR), especially around 70 μm (given typical dust temperatures; da Cunha et al. 2008). Since our systems are powerful IR-emitters (with median $\log(L_{IR}/L_\odot) = 11.4^{+0.6}_{-0.9}$), we assume that all the FUV photons are processed by dust and re-emitted at 70 μm.

We use *Herschel*/PACS 70 μm High Level Images[5] to extract a value for G_0, assuming that all FUV photons are absorbed by dust grains and re-emitted at 70 μm. To do so, we fit the radial profile of the 70 μm photometric map with a Sersic function:

$$F(R) = F_e \exp\left\{-b_n\left[\left(\frac{R}{R_e}\right)^{1/n} - 1\right]\right\}. \quad (6)$$

The free parameters of this fit are F_e, R_e, and n, while b_n is a constant that depends on n (Sérsic 1963). We then divide the normalization flux F_e by 1.6×10^{-3} erg cm^{-2} s^{-1}, obtaining a profile in G_0 units. In this way, we find values corresponding to the radius R_e, with median $\log G_0(R_e) = 2.6^{+0.5}_{-0.8}$, which is similar to what Farrah et al. (2013) and Díaz-Santos et al. (2017) found for local (U)LIRGs, in the HERUS ($10^{2.2} < G_0 < 10^{3.6}$) and the GOALS ($10^1 < G_0 < 10^{3.5}$) samples, respectively. It is important to note that in these works, as in most of the literature, G_0 is derived from PDR calculations fitting the observed line emission, thus relying on PDR codes as e.g. the PDR TOOLBOX (Pound & Wolfire 2008) and CLOUDY (Ferland et al. 2017). Here, instead, we observationally derive G_0 and we use the fitted profile to estimate its value at different radii. G_0 increases at smaller radii due to the higher SFR in the circumnuclear region, and the consequent high FUV irradiation. At $r = 250$ pc, we find a median $\log G_0(250\,\mathrm{pc}) = 3.1^{+0.7}_{-0.8}$. We look then for correlations between the CO line ratios and G_0 (from now on when we refer to G_0 values we mean measured at $r = 250$ pc), to understand if the FUV irradiation can explain by itself the observed CO emission at the centre of local active galaxies.

In Fig. 3, we show the CO(6–5)/CO(1–0), CO(8–7)/CO(1–0), and CO(13–12)/CO(1–0) luminosity ratios on the left-hand panel, and the CO(9–8)/CO(6–5), CO(11–10)/CO(6–5), and CO(13–12)/CO(6–5) ratios on the right-hand panel, as a function of G_0. All the other CO line ratios are presented in the Appendix A. We see an overall trend, for high-G_0 galaxies, to show increasing high-J/low-J and high-J/mid-J ratios.

We fit a regression line with the `Linmix` algorithm (Kelly 2007), which evaluates the likelihood in presence of censored data (i.e. upper limits). Linmix computes the likelihood function by convolving multiple (we use two, since adding more has a negligible effect on our results) hierarchical Gaussian distributions. We also tried to fit only the detections with an ordinary least squares regression and with a bootstrapped version of the same algorithm, finding limited differences with respect to the Linmix regression, which includes the censored data. Since an important fraction (between 20 and 50 per cent, depending on the transition) of the high-J CO fluxes are actually upper limits (see Table 2), we plot the Linmix results in Figs 3 and 4 and in Appendix A.

We find steeper slopes for the CO(1–0) ratios, and a trend of increasing steepness with J for both ratios. However, almost all the regression slopes return a sub-linear relation between the CO line ratios and G_0, with slopes 0.3–1.1 for the CO(1–0) ratios, and 0.1–0.4 for the CO(6–5) ratios. These findings suggest that the CO excitations are not strongly dependent on the radiative field G_0, and other excitation mechanisms may contribute to the CO line emission.

We also plot in Fig. 3 the median line ratios for the Milky Way (MW, Fixsen et al. 1999) and the AGN from the ASPECS (Walter et al. 2016) AGN sample (Boogaard et al. 2020). The MW has a lower CO ratio than most of our sources, which is expected since our galaxies are forming stars at a higher rate than the MW and host an AGN. The ASPECS AGNs are instead bright ($L_{IR} \sim 10^{12} L_\odot$) and have a median CO ratio comparable to our active galaxies. These

[5] https://irsa.ipac.caltech.edu/data/Herschel/HHLI/overview.html

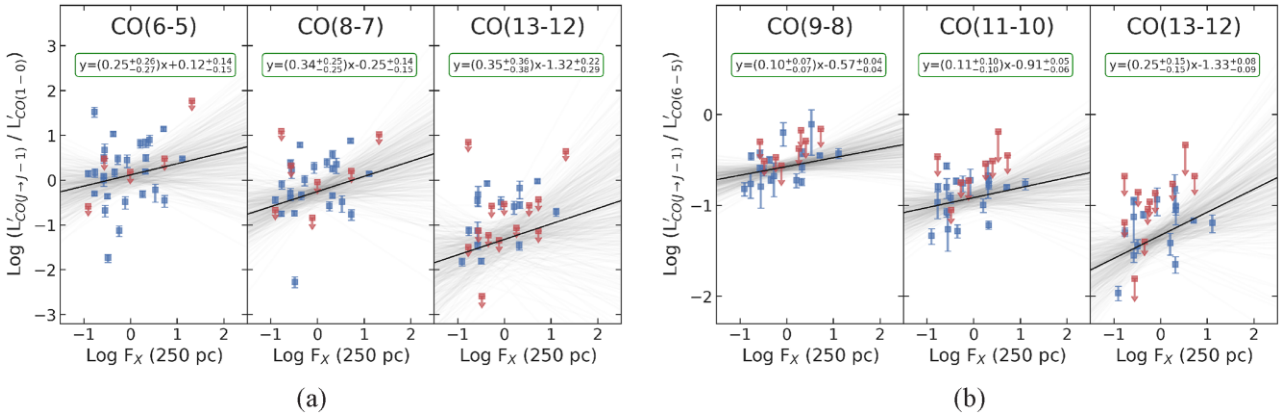

Figure 4. CO ratios as a function of F_X, in units of erg s^{-1} cm^{-2}, derived at $r = 250$ pc (see Section 5.2). We consider both the luminosity ratios $L'_{CO(J\rightarrow J-1)}/L'_{CO(1\rightarrow 0)}$ with respect to the CO(1–0) (left-hand panel, 4a) and $L'_{CO(J\rightarrow J-1)}/L'_{CO(6\rightarrow 5)}$ with respect to the CO(6–5) line luminosity (right-hand panel, 4b). The luminosities L' are in units of K km s^{-1} pc^{-2}, and J is indicated on the top of each panel. Blue squares indicate 3σ detections in both lines; red squares with downward arrow indicate $<3\sigma$ detections in the higher-J line. The solid black line is the regression fit, with the underlying grey lines showing the fits drawn from the posterior distribution.

AGN are located at $z \sim 1-3$, at the peak of the cosmic SF history (Madau & Dickinson 2014).

5.2 XDR

We use the L_X and N_H derived for our sample (see Section 3.1 for details) to estimate the unobscured X-ray flux, $F_X = L_X/(4\pi r^2)$, illuminating the GMCs located at $r = 250$ pc from the center of our galaxies. We find a median $\log(F_X/\mathrm{erg\ s^{-1}cm^{-2}}) = -0.1^{+0.8}_{-0.5}$.

According to theoretical (Kawakatu & Wada 2008) and observational works (Davies et al. 2007; Esquej et al. 2014; Motter et al. 2021), the circumnuclear star-forming region directly influenced by the AGN has a ≈100 pc radius. However, with the available ALMA data (Section 3.3) we could study only up to the mid-J CO(6–5) emission, which is confined, on average, within a ∼250 pc radius. We, therefore, calculate our X-ray fluxes at this $r = 250$ pc. It is also possible to estimate F_X from XDR numerical modelling, as done by van der Werf et al. (2010), Pozzi et al. (2017), and Mingozzi et al. (2018). Those works all find higher F_X than ours for three galaxies of our sample (respectively Mrk 231, NGC 7130, and NGC 34). This may imply that $r = 250$ pc is a too large radius for the central XDR.

The X-ray flux F_X does not account for the obscuration of the X-ray photons before they strike the molecular gas. It is therefore useful to calculate the local (i.e. accounting for the absorption) X-ray energy deposition rate per particle H_X. It can be estimated from the following formula (Maloney et al. 1996):

$$H_X \approx 7 \times 10^{-22} L_{44}\, r_2^{-2} N_{22}^{-1} \ \ \mathrm{erg\ s^{-1}}, \tag{7}$$

where the X-ray luminosity is $L_X = 10^{44} L_{44}$ erg s^{-1}, the distance to the X-ray source is $r = 10^2 r_2$ pc and the attenuating column density is $N_H = 10^{22} N_{22}$ cm^{-2}. We find a median $\log(H_X/(\mathrm{erg\ s^{-1}}) = -25.3^{+1.1}_{-0.9}$. We use the N_H measured from the X-ray spectrum (Section 3.1) to estimate H_X. Although a Compton-thick gas ($N_H > 10^{24}$ cm^{-2}) is generally associated to small-scale structures like a dusty molecular torus, Compton-thin gas (as it is for 65 per cent of our sample) may be part of the same circumnuclear gas we are studying from molecular and IR emission (Ballantyne 2008; Hickox & Alexander 2018). In this case, the $H_X \propto N_H^{-1}$ we calculate from equation (7) could be underestimated, since there would be a lower N_H between the XDR and the AGN.

A key physical quantity affecting the XDR emission, and directly proportional to H_X/n, is the effective ionization parameter, defined (Maloney et al. 1996; Galliano et al. 2003; Motter et al. 2021) as

$$\xi_{\mathrm{eff}} = 1.06 \times 10^{-2} L_{44}\, r_2^{-2}\, N_{22}^{-\alpha}\, n_5^{-1} \ \ \mathrm{erg\ cm^3\ s^{-1}}, \tag{8}$$

where the density of the XDR gas is $n = 10^5 n_5$ cm^{-3}, $\alpha = (\Gamma + 2/3)/(8/3)$ depends on the photon index Γ of the X-ray spectrum (Kawamuro et al. 2020) and the other quantities are the same defined above for H_X. For a representative fixed value of $n_5 = 0.1$, we find a median $\log \xi_{\mathrm{eff}}/(\mathrm{erg\ cm^3 s^{-1}}) = -4.2^{+1.9}_{-1.0}$. These values are very low when compared to the theoretical values found in Maloney et al. (1996) models (e.g. their fig. 7) and to the observed values found in Motter et al. (2021), who calculated ξ_{eff} for the active galaxy NGC 34, also present in our sample. Motter et al. (2021) used N_H derived from radio observations (which is 1 dex lower than the one we use for NGC 34, derived from X-rays), and calculated ξ_{eff} at distances from the AGN between 40 and 120 pc, thus finding values ∼2 dex higher than us. When taking into account these differences, the results are compatible. Again, this may be a clue that at $r = 250$ pc we cannot yet see the AGN impact.

In Fig. 4, we plot the same luminosity line ratios [CO(6–5)/CO(1–0), CO(8–7)/CO(1–0), and CO(13–12)/CO(1–0) on the left-hand panel; CO(9–8)/CO(6–5), CO(11–10)/CO(6–5), and CO(13–12)/CO(6–5) on the right-hand panel] analysed in Fig. 3, as a function of F_X only, since both H_X and ξ_{eff} were showing, compared to F_X, less defined trends. The other CO line ratios and their regression fits, as function of F_X, are presented in Appendix A.

Compared to the PDR results shown in Fig. 3, for the XDR we find lower regression slopes: 0.1–0.5 for the CO(1–0) ratios and 0–0.2 for the CO(6–5) ratios. We interpret this as a sign that neither F_X is the dominant driver of these CO lines. Given the physics of high-J CO line emission, which originate from warm molecular gas, the X-ray influence was expected to show up in the correlation with the line ratios, especially those with respect to the low-J CO lines, as found by many theoretical (Maloney et al. 1996; Meijerink & Spaans 2005; Meijerink et al. 2007) and observational (van der Werf et al. 2010; Pozzi et al. 2017; Mingozzi et al. 2018) works on XDR. A plausible explanation is that at $r = 250$ pc we are still outside of the actual AGN sphere of influence of the molecular gas: several studies on Seyfert galaxies (Davies et al. 2007; Kawakatu & Wada 2008; Esquej et al.

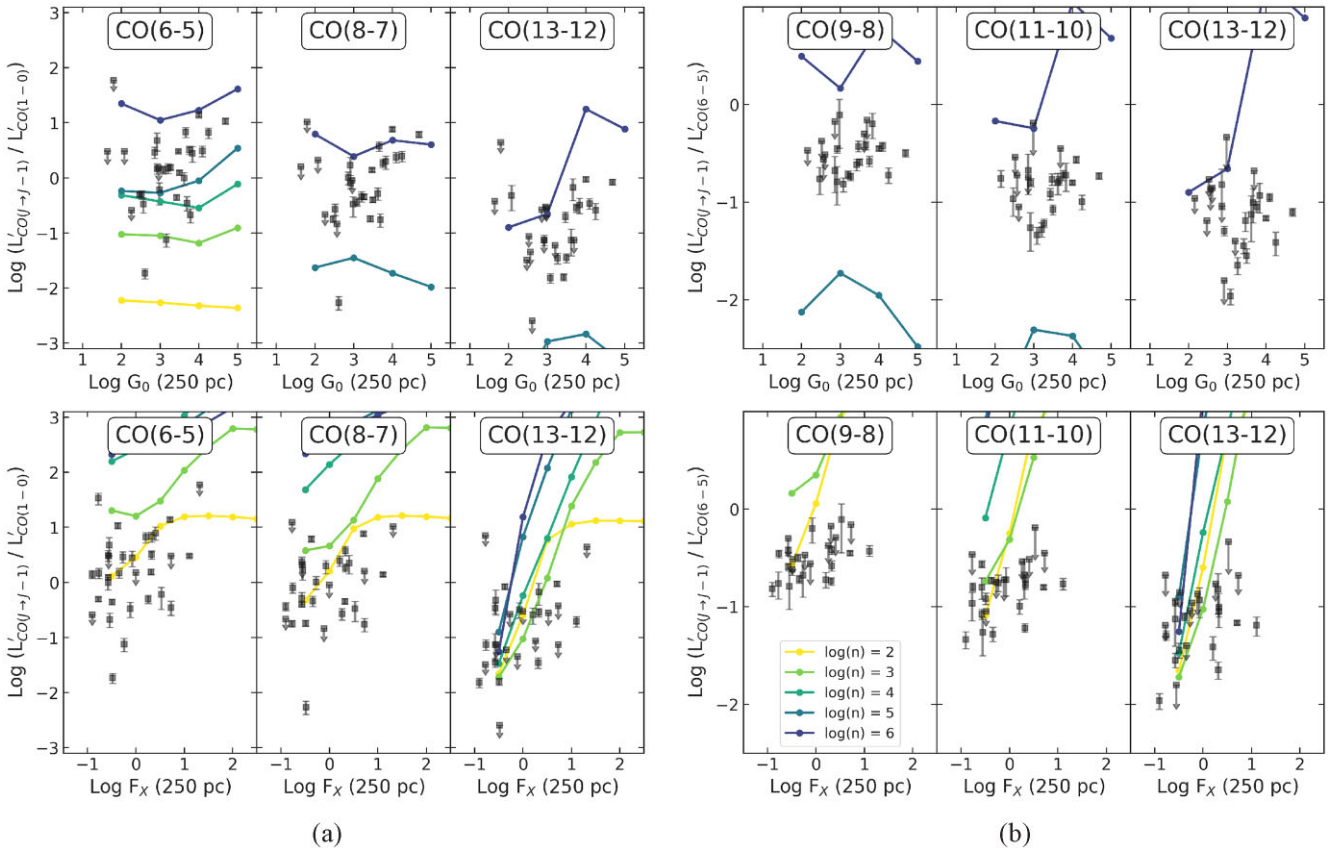

Figure 5. *Top-left*: G_0 versus CO ratio to the nuclear ($r = 250$ pc) fraction of CO(1–0). *Top-right*: G_0 versus CO ratio to the CO(6–5) line. *Bottom-left*: F_X versus CO ratio to the nuclear ($r = 250$ pc) fraction of CO(1–0). *Bottom-right*: F_X versus CO ratio to the CO(6–5) line. In all the plots, the points are the same of Figs 3 and 4. Both G_0 and F_X are measured at $r = 250$ pc. The coloured overplotted lines are from numerical CLOUDY models of different gas densities n, namely 10^2 (yellow), 10^3 (light green), 10^4 (aqua green), 10^5 (light blue), and 10^6 (dark blue) cm^{-3}.

2014; Motter et al. 2021) indeed place it within the central $r = 100$ pc. At larger radii, we cannot isolate the contribution of X-rays due to dilution with stellar FUV photons. Unfortunately, our *Herschel* CO observations have limited spatial resolution to reach such a nuclear region, and ALMA is still limited to the low/mid-J lines, at least in the local Universe.

5.3 Comparison with models

We use predictions from numerical models presented in Vallini et al. (2019) to interpret the observations, in order to shed light on the dominant heating source in the molecular ISM of our galaxies. For this purpose, we use CLOUDY (Ferland et al. 2017) to compute the CO line intensities emerging from a 1D gas slab of density n, illuminated by either FUV flux G_0 (PDR models) or a X-ray flux F_X (XDR models). The results of these simulations mainly apply for a single cloud, while we are dealing with entire galaxies (or at least their inner regions); it is therefore especially convenient to study the effect on the line ratios, rather than line fluxes or luminosities, assuming that both numerators and denominators originate from the same area.

The gas density n is a fundamental missing quantity in our analysis of PDR and XDR. We do have some indications of its possible value: from the X-ray-derived column density, we estimated mean volume densities between $n \approx 10^{1-3}$ cm^{-3} (Section 3.1) within $r = 250$ pc. It is however possible, from the comparison of observed CO ratios with PDR and XDR CLOUDY models outputs, to estimate the density of the dissociation region from which the observed CO lines originate.

In the four panels of Fig. 5, we examine the PDR and XDR predictions, respectively, made with $\log G_0 = [2, 3, 4, 5]$ and $\log (F_X/(\mathrm{erg\ s^{-1} cm^{-2}})) = [-0.5, 0, 0.5, 1, 1.5, 2, 2.5]$, with modelled gas density $\log (n/\mathrm{cm^{-3}}) = [2, 3, 4, 5]$. Again we explore the CO line ratio to CO(1–0) and CO(6–5), using the same three mid-/high-J lines as in Figs 3 and 4. The same plots with all the CO lines can be found at the end of Appendix A (Figs A5–A8). The modelled points are plotted in the panels of Fig. 5, colour coded with n.

In the PDR case, almost all our galaxies are reproduced considering densities in the $n = 10^{5-6}$ cm^{-3} range, except for the line ratios up to CO(6–5), as can be seen on the leftmost panel ($L'_{\mathrm{CO(6-5)}}/L'_{\mathrm{CO(1-0)}}$) of Fig. 5, and even better in the first lines of Figs A5 and A6. Previous PDR studies did not find such high densities. The only exception is Mrk 231, for which van der Werf et al. (2010) obtained a warm PDR component with $G_0 = 10^{3.5}$ and $n = 10^5$ cm^{-3}; however, such a high density is necessary to reproduce the mid-J emission, while a colder PDR component, with $n = 10^{3.5}$ cm^{-3}, reproduces the low-J emission and accounts for most of the gas volume. Díaz-Santos et al. (2017) observed instead that on average, and on the scale of the whole galaxy, local (U)LIRGs start from a minimum $G_0/n \sim 10^{-1}$, and that this ratio increases with the IR luminosity surface density; this would place an upper limit to the gas density at a fixed G_0. In the top panels of Fig. 5, instead, our galaxies, for $J_{\mathrm{upp}} \geq 8$, lie in the range $\log (G_0/n) = [-4, -1]$, given the modelled gas densities. It is necessary for PDR models to have high densities to produce bright mid-J transitions (Vallini et al. 2018), and it is known (e.g. McKee & Ostriker 2007) that such densities are typical of clumps and cores in

single star-forming molecular clouds (as shown by Joblin et al. 2018, in e.g. the Orion Bar). None the less, it is unlikely that the central 500 pc of galaxies have an average gas density of 10^{5-6} cm^{-3}, so we expect these high-density regions to have a very low volume filling factor.

In the XDR case, on the contrary, the models with low density ($n \approx 10^{2-3}$ cm^{-3}) can reproduce the observed CO line ratios, at least in the regions of the parameters space where the lines with such densities are clearly separable from the others. This result is in line with the densities ($n \approx 10^{1-3}$ cm^{-3}) calculated from the X-ray-derived $N_{\rm H}$, and from what we expect from the available XDR studies for local (U)LIRGs (van der Werf et al. 2010; Pozzi et al. 2017; Mingozzi et al. 2018). From Fig. 5, it is clear that the observed high-J line ratios (especially $J_{\rm upp} \geq 12$) can be reproduced by either a high F_X or a high n, a degeneracy also found in the semi-analytic model by Vallini et al. (2019). However, both our high-J line ratios and our calculated $F_{\rm X}$ are lowered by the nuclear radius we are using ($r = 250$ pc), so a detailed numerical modelling at different distances from the AGN is needed to really see the impact of XDR on the molecular emission.

We note here that stars and AGN can also affect the heating of molecular gas through outflows/winds, resulting in shock-heated regions (Aalto et al. 2012; Kazandjian et al. 2012; García-Burillo et al. 2014) where the brightness of high-J CO lines is enhanced too. Disentangling the contribution of shock heating from that produced in XDRs is a challenging task (Hollenbach & McKee 1989; Meijerink et al. 2013; Mingozzi et al. 2018). However, the study of mechanical heating is beyond the scope of this paper.

6 CONCLUSIONS

In this paper, we investigate the relative impact of star formation and AGN activity on the CO rotational line emission. In this respect, we collect multiwavelength (mm, IR and X-ray) data for a sample of 35 local active galaxies. The sources are selected with a well-sampled CO SLED (from $J = 1{-}0$ to $J = 13{-}12$) and intrinsic $L_X \geq 10^{42}$ erg s^{-1} in the 2–10 keV range. From the multiband data we derive, in a homogeneous way, key integrated physical quantities, as the molecular gas mass ($M_{\rm mol}$), the star formation FUV flux (G_0), and the AGN X-ray flux, $F_{\rm X}$. Moreover, by analysing the ALMA images of the highest available CO emission, we estimate the emitting area of mid-J/high-J CO lines, finding it concentrated within $r = 250$ pc from the center. To determine whether AGN activity influences the molecular gas in its vicinity, we measure FUV and X-ray radiation, producing PDR and XDR, respectively, from the observational data in a self-consistent way. The FUV flux is parametrized in terms of G_0, gauged from the 70 μm, spatially resolved, dust emission, the F_X is calculated from the intrinsic L_X. Our main results can be summarized as follows:

(1) On the kpc-scale of the whole galaxy (namely within a median $r_{\rm CO} = 3.1^{+2.1}_{-1.5}$ kpc), we do not find measurable evidence for the AGN influence on the star formation. Our sample results well mixed with other samples of non-active galaxies on the Schmidt–Kennicutt ($\Sigma_{\rm mol}$ versus $\Sigma_{\rm SFR}$) plane. If we use a Milky Way CO-to-H$_2$ conversion factor $\alpha_{\rm CO} = 4.3$ M$_\odot$ (K km s^{-1} pc^{-2})$^{-1}$, we find a median $\log(M_{\rm mol}/M_\odot) = 9.9^{+0.3}_{-0.8}$ for our sample, and a median depletion time $\log(\tau_{\rm depl}/{\rm yr}) = 8.9^{+0.4}_{-0.6}$.

(2) We measure within $r = 250$ pc the irradiation of PDR and XDR by deriving G_0 and F_X, finding $\log G_0 = 3.1^{+0.7}_{-0.8}$ and $\log(F_{\rm X}/({\rm erg\ s^{-1}cm^{-2}})) = -0.1^{+0.8}_{-0.5}$ for our sample. These values are comparable with the literature for local active galaxies for both observational and theoretical works.

(3) We find weak correlations between G_0, $F_{\rm X}$ and two different CO line ratios, namely to the nuclear ($r = 250$ pc) fraction of CO(1–0) and to CO(6–5). Therefore, neither G_0 nor $F_{\rm X}$ alone can produce the observed molecular emission.

(4) From the comparison of CO emission and observed G_0 with grids of PDR numerical models, we can conclude that PDR emission can reproduce observed high-J line ratios only assuming unlikely extreme gas densities ($n > 10^5$ cm^{-3}), while it is more efficient at moderate densities ($n \sim 10^{3-4}$ cm^{-3}) up to CO(6–5).

(5) From the comparison between XDR observations and models, we find that $F_{\rm X}$ can reproduce the observed low-/mid-J CO line ratios only at low densities ($n \sim 10^2$ cm^{-3}), similar to those estimated from X-ray column densities ($n \sim 10^{1-3}$ cm^{-3}). At high-J, we find increasing (with J) degeneracy between $F_{\rm X}$ and n, so we cannot find a typical gas density for our sample. This is probably an indication that the nuclear scale at which we are considering the XDR is still too large to see a strong AGN effect on the CO SLED.

From our analysis, we conclude that, on scales of ≈250 pc from the galaxy center, a mix of PDR and XDR is necessary to explain the observed CO emission, since neither of them is the dominant mechanism. The use of the CO SLED to disentangle the contribution of FUV and/or X-rays photons to the molecular gas heating in local galaxies is currently limited by the low spatial resolution at the high-J frequencies (∼17 arcsec for CO(13–12) with *Herschel*/PACS). Conversely, high-z galaxies have their high-J CO emission redshifted into the observation bands of ALMA and NOEMA, which are able to reach sub-arcsec resolution. These extreme CO lines have been observed and modelled already by several works (Gallerani et al. 2014; Carniani et al. 2019; Pensabene et al. 2021). It would be therefore interesting to extend the analysis performed in this paper on a high-redshift sample of active galaxies with spatially resolved CO emission, and assess possible differences with local AGN.

ACKNOWLEDGEMENTS

We acknowledge use of APLPY (Robitaille & Bressert 2012; Robitaille 2019), ASTROPY (Astropy Collaboration et al. 2013, 2018), MATPLOTLIB (Hunter 2007), NUMPY (Harris et al. 2020), PANDAS (The pandas development team 2020), PHOTUTILS (Bradley et al. 2020), PYTHON (Van Rossum & Drake 2009), SEABORN (Waskom 2021), SCIKIT-LEARN (Pedregosa et al. 2011), and SCIPY (Virtanen et al. 2020). This research has made use of the NASA/IPAC Extragalactic Database (NED), which is funded by the National Aeronautics and Space Administration and operated by the California Institute of Technology. We acknowledge the usage of the HyperLeda data base (http://leda.univ-lyon1.fr; Makarov et al. 2014). Optical images of galaxies are based on observations made with the NASA/ESA *Hubble Space Telescope*, and obtained from the Hubble Legacy Archive, which is a collaboration between the Space Telescope Science Institute (STScI/NASA), the Space Telescope European Coordinating Facility (ST-ECF/ESA) and the Canadian Astronomy Data Centre (CADC/NRC/CSA). This research has made use of the services of the ESO Science Archive Facility. We acknowledge the use of DSS (Digitized Sky Survey) images. This paper makes use of the following ALMA data: ADS/JAO.ALMA\#2011.0.00083.S, 2011.0.00182.S, 2012.1.00225.S, 2013.1.00014.S, 2013.1.00524.S, 2015.1.00658.S, and 2016.1.01223.S. ALMA is a partnership of ESO (representing its member states), NSF (USA) and NINS (Japan),

together with NRC (Canada), MOST and ASIAA (Taiwan), and KASI (Republic of Korea), in cooperation with the Republic of Chile. The Joint ALMA Observatory is operated by ESO, AUI/NRAO and NAOJ. Part of the ALMA data are retrieved from the JVO portal (http://jvo.nao.ac.jp/portal) operated by the NAOJ. The DSS was produced at the Space Telescope Science Institute under US Government grant NAG W-2166. The images of these surveys are based on photographic data obtained using the Oschin Schmidt Telescope on Palomar Mountain and the UK Schmidt Telescope. This research has made use of Aladin Sky Atlas developed at CDS, Strasbourg Observatory, France (Bonnarel et al. 2000; Boch & Fernique 2014). FE and FP acknowledge support from grant PRIN MIUR 2017- 20173ML3WW_001. We acknowledge support from the INAF mainstream 2018 programme 'Gas-DustPedia: A definitive view of the ISM in the Local Universe'.

DATA AVAILABILITY

The data underlying this article were accessed from the ALMA Archive (https://almascience.eso.org/asax/), from the JVO portal (http://jvo.nao.ac.jp/portal) operated by the NAOJ, and the NASA/IPAC Infrared Science Archive (specifically https://irsa.ipac.caltech.edu/data/Herschel/HHLI/overview.html), which is funded by the National Aeronautics and Space Administration and operated by the California Institute of Technology The derived data generated in this research will be shared on reasonable request to the corresponding author.

REFERENCES

Aalto S., Booth R. S., Black J. H., Johansson L. E. B., 1995, A&A, 300, 369
Aalto S., Garcia-Burillo S., Muller S., Winters J. M., van der Werf P., Henkel C., Costagliola F., Neri R., 2012, A&A, 537, A44
Albrecht M., Krügel E., Chini R., 2007, A&A, 462, 575
Alloin D., Barvainis R., Gordon M. A., Antonucci R. R. J., 1992, A&A, 265, 429
Alonso-Herrero A. et al., 2011, ApJ, 736, 82
Alonso-Herrero A., Pereira-Santaella M., Rieke G. H., Rigopoulou D., 2012, ApJ, 744, 2
Astropy Collaboration et al., 2013, A&A, 558, A33
Astropy Collaboration et al., 2018, AJ, 156, 123
Ballantyne D. R., 2008, ApJ, 685, 787
Barthelmy S. D. et al., 2005, Space Sci. Rev., 120, 143
Bellocchi E., Arribas S., Colina L., 2016, A&A, 591, A85
Bendo G. J., Clements D. L., Khan S. A., 2009, MNRAS, 399, L29
Bianchi S., Chiaberge M., Piconcelli E., Guainazzi M., Matt G., 2008, MNRAS, 386, 105
Bigiel F., Leroy A., Walter F., Brinks E., de Blok W. J. G., Madore B., Thornley M. D., 2008, AJ, 136, 2846
Boch T., Fernique P., 2014, in Manset N., Forshay P., eds, ASP Conf. Ser. Vol. 485, Astronomical Data Analysis Software and Systems XXIII. Astron. Soc. Pac., San Francisco, p. 277
Bolatto A. D., Wolfire M., Leroy A. K., 2013, ARA&A, 51, 207
Bonnarel F. et al., 2000, A&AS, 143, 33
Boogaard L. A. et al., 2020, ApJ, 902, 109
Boselli A., Cortese L., Boquien M., 2014, A&A, 564, A65
Bradley L. et al., 2020, astropy/photutils: 1.0.0. Zenodo. Available at: https://doi.org/10.5281/zenodo.4044744
Brightman M., Nandra K., 2011, MNRAS, 413, 1206
Buchner J., Bauer F. E., 2017, MNRAS, 465, 4348
Calura F., Gilli R., Vignali C., Pozzi F., Pipino A., Matteucci F., 2014, MNRAS, 438, 2765
Calzetti D. et al., 2010, ApJ, 714, 1256
Carilli C. L., Walter F., 2013, ARA&A, 51, 105
Carniani S. et al., 2019, MNRAS, 489, 3939
Casasola V. et al., 2017, A&A, 605, A18
Casasola V., Bettoni D., Galletta G., 2004, A&A, 422, 941
Casasola V., Hunt L., Combes F., García-Burillo S., 2015, A&A, 577, A135
Casasola V. et al., 2020, A&A, 633, A100
Comastri A., 2004, in Barger A. J., ed., Astrophysics and Space Science Library, Vol. 308, Supermassive Black Holes in the Distant Universe. Kluwer Academic Publishers, Dordrecht, p. 245
Combes F., Prugniel P., Rampazzo R., Sulentic J. W., 1994, A&A, 281, 725
Curran S. J., Polatidis A. G., Aalto S., Booth R. S., 2001, A&A, 368, 824
D'Amato Q. et al., 2020, A&A, 636, A37
da Cunha E., Charlot S., Elbaz D., 2008, MNRAS, 388, 1595
Dasyra K. M., Combes F., Oosterloo T., Oonk J. B. R., Morganti R., Salomé P., Vlahakis N., 2016, A&A, 595, L7
Davies R. I., Müller Sánchez F., Genzel R., Tacconi L. J., Hicks E. K. S., Friedrich S., Sternberg A., 2007, ApJ, 671, 1388
Decarli R. et al., 2020, ApJ, 902, 110
Díaz-Santos T. et al., 2017, ApJ, 846, 32
Downes D., Solomon P. M., 1998, ApJ, 507, 615
Dumas G., Schinnerer E., Mundell C. G., 2010, ApJ, 721, 911
Dunne L., Eales S., Edmunds M., Ivison R., Alexander P., Clements D. L., 2000, MNRAS, 315, 115
Ellison S. L., Viswanathan A., Patton D. R., Bottrell C., McConnachie A. W., Gwyn S., Cuillandre J.-C., 2019, MNRAS, 487, 2491
Espada D. et al., 2017, ApJ, 843, 136
Espada D. et al., 2019, ApJ, 887, 88
Esquej P. et al., 2014, ApJ, 780, 86
Evans A., 2005, An ACS Survey of a Complete Sample of Luminous Infrared Galaxies in the Local Universe. HST Proposal ID 10592
Evans A. S., Mazzarella J. M., Surace J. A., Frayer D. T., Iwasawa K., Sanders D. B., 2005, ApJS, 159, 197
Farrah D. et al., 2013, ApJ, 776, 38
Feltre A., Hatziminaoglou E., Fritz J., Franceschini A., 2012, MNRAS, 426, 120
Ferland G. J. et al., 2017, Rev. Mex. Astron. Astrofis., 53, 385
Fixsen D. J., Bennett C. L., Mather J. C., 1999, ApJ, 526, 207
Flower D. R., Pineau Des Forêts G., 2010, MNRAS, 406, 1745
Gallerani S., Ferrara A., Neri R., Maiolino R., 2014, MNRAS, 445, 2848
Galliano E., Alloin D., Granato G. L., Villar-Martín M., 2003, A&A, 412, 615
Gao Y., Solomon P. M., 1999, ApJ, 512, L99
Gao Y., Solomon P. M., 2004, ApJS, 152, 63
García-Burillo S. et al., 2003, A&A, 407, 485
García-Burillo S. et al., 2014, A&A, 567, A125
Gehrels N. et al., 2004, ApJ, 611, 1005
Gerssen J., van der Marel R. P., Axon D., Mihos J. C., Hernquist L., Barnes J. E., 2004, AJ, 127, 75
Golombek D., Miley G. K., Neugebauer G., 1988, AJ, 95, 26
Greve T. R. et al., 2014, ApJ, 794, 142
Griffin M. J. et al., 2010, A&A, 518, L3
Gruppioni C. et al., 2016, MNRAS, 458, 4297
Habing H. J., 1968, Bull. Astron. Inst. Netherlands, 19, 421
Harris C. R. et al., 2020, Nature, 585, 357
Harrison F. A. et al., 2013, ApJ, 770, 103
Hatziminaoglou E. et al., 2008, MNRAS, 386, 1252
Heckman T. M., Best P. N., 2014, ARA&A, 52, 589
Hickox R. C., Alexander D. M., 2018, ARA&A, 56, 625
Hollenbach D., McKee C. F., 1989, ApJ, 342, 306
Hollenbach D. J., Tielens A. G. G. M., 1997, ARA&A, 35, 179
Hollenbach D. J., Tielens A. G. G. M., 1999, Rev. Mod. Phys., 71, 173
Hopkins P. F., Hernquist L., Cox T. J., Kereš D., 2008, ApJS, 175, 356
Hung C.-L. et al., 2014, ApJ, 791, 63
Hunter J. D., 2007, Comput. Sci. Eng., 9, 90
Imanishi M., Ichikawa K., Takeuchi T., Kawakatu N., Oi N., Imase K., 2011, PASJ, 63, 447
Imanishi M., Nakanishi K., Izumi T., 2016, AJ, 152, 218
Imanishi M., Nakanishi K., Izumi T., 2017, ApJ, 849, 29
Israel F. P., 1992, A&A, 265, 487

Israel F. P., 2020, A&A, 635, A131
Joblin C. et al., 2018, A&A, 615, A129
Kamenetzky J., Rangwala N., Glenn J., Maloney P. R., Conley A., 2014, ApJ, 795, 174
Kamenetzky J., Rangwala N., Glenn J., Maloney P. R., Conley A., 2016, ApJ, 829, 93
Kawakatu N., Wada K., 2008, ApJ, 681, 73
Kawamuro T., Izumi T., Onishi K., Imanishi M., Nguyen D. D., Baba S., 2020, ApJ, 895, 135
Kazandjian M. V., Meijerink R., Pelupessy I., Israel F. P., Spaans M., 2012, A&A, 542, A65
Kelly B. C., 2007, ApJ, 665, 1489
Kennicutt R. C., Jr, 1998, ApJ, 498, 541
Kennicutt R. C., Jr, De Los Reyes M. A. C., 2021, ApJ, 908, 61 (K21)
Kennicutt R. C., Evans N. J., 2012, ARA&A, 50, 531
Kojoian G., Elliott R., Tovmassian H. M., 1981, AJ, 86, 811
Komossa S., Burwitz V., Hasinger G., Predehl P., Kaastra J. S., Ikebe Y., 2003, ApJ, 582, L15
Koss M. J. et al., 2016, ApJ, 824, L4
Koss M. J. et al., 2021, ApJS, 252, 29
Krimm H. A. et al., 2013, ApJS, 209, 14
La Caria M. M., Vignali C., Lanzuisi G., Gruppioni C., Pozzi F., 2019, MNRAS, 487, 1662
Lamperti I. et al., 2020, ApJ, 889, 103 (L20)
Larson K. L. et al., 2016, ApJ, 825, 128
Larson R. B., Tinsley B. M., 1978, ApJ, 219, 46
Leroy A. K., Walter F., Brinks E., Bigiel F., de Blok W. J. G., Madore B., Thornley M. D., 2008, AJ, 136, 2782
Leroy A. K. et al., 2021, ApJS, 257, 43
Leslie S. K., Rich J. A., Kewley L. J., Dopita M. A., 2014, MNRAS, 444, 1842
Lisenfeld U. et al., 2011, A&A, 534, A102
Lonsdale C. J., Farrah D., Smith H. E., 2006, in Mason J. W., ed., Astrophysics Update 2. Praxis Publishing Ltd, Chichester, p. 285
Lu N. et al., 2017, ApJS, 230, 1
McKee C. F., Ostriker E. C., 2007, ARA&A, 45, 565
McMullin J. P., Waters B., Schiebel D., Young W., Golap K., 2007, in Shaw R. A., Hill F., Bell D. J., eds, ASP Conf. Ser. Vol. 376, Astronomical Data Analysis Software and Systems XVI. Astron. Soc. Pac., San Francisco, p. 127
Madau P., Dickinson M., 2014, ARA&A, 52, 415
Maiolino R., Ruiz M., Rieke G. H., Papadopoulos P., 1997, ApJ, 485, 552
Makarov D., Prugniel P., Terekhova N., Courtois H., Vauglin I., 2014, A&A, 570, A13
Malkan M. A., Gorjian V., Tam R., 1998, ApJS, 117, 25
Maloney P. R., Hollenbach D. J., Tielens A. G. G. M., 1996, ApJ, 466, 561
Mao R.-Q., Schulz A., Henkel C., Mauersberger R., Muders D., Dinh-V-Trung, 2010, ApJ, 724, 1336
Marchesi S. et al., 2019, ApJ, 872, 8
Marconi A., Schreier E. J., Koekemoer A., Capetti A., Axon D., Macchetto D., Caon N., 2000, ApJ, 528, 276
Mashian N. et al., 2015, ApJ, 802, 81
Matt G., Fabian A. C., Guainazzi M., Iwasawa K., Bassani L., Malaguti G., 2000, MNRAS, 318, 173
Meijerink R., Spaans M., 2005, A&A, 436, 397
Meijerink R., Spaans M., Israel F. P., 2007, A&A, 461, 793
Meijerink R. et al., 2013, ApJ, 762, L16
Merkulova O. A., Karataeva G. M., Yakovleva V. A., Burenkov A. N., 2012, Astron. Lett., 38, 290
Michiyama T. et al., 2021, ApJS, 257, 28
Mingozzi M. et al., 2018, MNRAS, 474, 3640
Monje R. R., Blain A. W., Phillips T. G., 2011, ApJS, 195, 23
Moreno J. et al., 2019, MNRAS, 485, 1320
Morrison R., McCammon D., 1983, ApJ, 270, 119
Moshir M. et al., 1990, BAAS, 22, 1325
Motter J. C. et al., 2021, MNRAS, 506, 4354
Mundell C. G., James P. A., Loiseau N., Schinnerer E., Forbes D. A., 2004, ApJ, 614, 648
Narayanan D., Krumholz M. R., 2014, MNRAS, 442, 1411
Netzer H., 2015, ARA&A, 53, 365
Omont A., 2007, Rep. Progr. Phys., 70, 1099
Oosterloo T., Morganti R., Tadhunter C., Raymond Oonk J. B., Bignall H. E., Tzioumis T., Reynolds C., 2019, A&A, 632, A66
Osterbrock D. E., Ferland G. J., eds, 2006, Astrophysics of Gaseous Nebulae and Active Galactic Nuclei, 2nd edn. University Science Books, Sausalito, CA
Pan H.-A. et al., 2018, ApJ, 868, 132
Papadopoulos P. P., van der Werf P. P., Xilouris E. M., Isaak K. G., Gao Y., Mühle S., 2012, MNRAS, 426, 2601
Pearson C. et al., 2016, ApJS, 227, 9
Pedregosa F. et al., 2011, J. Mach. Learn. Res., 12, 2825
Pensabene A. et al., 2021, A&A, 652, A66
Pereira-Santaella M. et al., 2013, ApJ, 768, 55
Pérez-Torres M., Mattila S., Alonso-Herrero A., Aalto S., Efstathiou A., 2021, A&AR, 29, 2
Perna M., Cresci G., Brusa M., Lanzuisi G., Concas A., Mainieri V., Mannucci F., Marconi A., 2019, A&A, 623, A171
Pilbratt G. L. et al., 2010, A&A, 518, L1
Poglitsch A. et al., 2010, A&A, 518, L2
Pound M. W., Wolfire M. G., 2008, in Argyle R. W., Bunclark P. S., Lewis J. R., eds, ASP Conf. Ser. Vol. 394, Astronomical Data Analysis Software and Systems XVII. Astron. Soc. Pac., San Francisco, p. 654
Pozzi F. et al., 2010, A&A, 517, A11
Pozzi F., Vallini L., Vignali C., Talia M., Gruppioni C., Mingozzi M., Massardi M., Andreani P., 2017, MNRAS, 470, L64
Ramos Almeida C., Ricci C., 2017, Nature Astron., 1, 679
Reynolds C. S., 1997, MNRAS, 286, 513
Ricci C. et al., 2017a, ApJS, 233, 17
Ricci C. et al., 2017b, MNRAS, 468, 1273
Rigopoulou D., Papadakis I., Lawrence A., Ward M., 1997, A&A, 327, 493
Robitaille T., 2019, APLpy v2.0: The Astronomical Plotting Library in Python. Zenodo. Available at: https://doi.org/10.5281/zenodo.2567476
Robitaille T., Bressert E., 2012, Astrophysics Source Code Library, record ascl:1208.017
Rosario D. J. et al., 2018, MNRAS, 473, 5658
Rosenberg M. J. F. et al., 2015, ApJ, 801, 72
Sabatini G., Gruppioni C., Massardi M., Giannetti A., Burkutean S., Cimatti A., Pozzi F., Talia M., 2018, MNRAS, 476, 5417
Saintonge A. et al., 2017, ApJS, 233, 22
Salomé P., Combes F., Revaz Y., Downes D., Edge A. C., Fabian A. C., 2011, A&A, 531, A85
Salvestrini F., Gruppioni C., Pozzi F., Vignali C., Giannetti A., Paladino R., Hatziminaoglou E., 2020, A&A, 641, A151
Sanders D. B., Mazzarella J. M., Kim D. C., Surace J. A., Soifer B. T., 2003, AJ, 126, 1607
Schleicher D. R. G., Spaans M., Klessen R. S., 2010, A&A, 513, A7
Schmidt M., 1959, ApJ, 129, 243
Schruba A. et al., 2011, AJ, 142, 37
Sérsic J. L., 1963, Boletin de la Asociacion Argentina de Astronomia La Plata Argentina, 6, 41
Singh V., Shastri P., Risaliti G., 2011, A&A, 532, A84
Tacconi L. J., Genzel R., Sternberg A., 2020, ARA&A, 58, 157
Talia M. et al., 2018, MNRAS, 476, 3956
Temporin S., Ciroi S., Rafanelli P., Radovich M., Vennik J., Richter G. M., Birkle K., 2003, ApJS, 148, 353
The pandas development team, 2020, pandas-dev/pandas: Pandas. Zenodo. Available at: https://doi.org/10.5281/zenodo.3509134
Treister E., Schawinski K., Urry C. M., Simmons B. D., 2012, ApJ, 758, L39
Ueda J. et al., 2014, ApJS, 214, 1
Utomo D. et al., 2018, ApJ, 861, L18
Vallini L., Pallottini A., Ferrara A., Gallerani S., Sobacchi E., Behrens C., 2018, MNRAS, 473, 271
Vallini L., Tielens A. G. G. M., Pallottini A., Gallerani S., Gruppioni C., Carniani S., Pozzi F., Talia M., 2019, MNRAS, 490, 4502
van der Werf P. P. et al., 2010, A&A, 518, L42

Van Rossum G., Drake F. L., 2009, Python 3 Reference Manual. CreateSpace, Scotts Valley, CA
Villanueva V. et al., 2021, ApJ, 923, 60
Virtanen P. et al., 2020, Nature Methods, 17, 261
Walter F. et al., 2016, ApJ, 833, 67
Waskom M. L., 2021, J. Open Source Softw., 6, 3021
Westmoquette M. S., Clements D. L., Bendo G. J., Khan S. A., 2012, MNRAS, 424, 416
Wilms J., Allen A., McCray R., 2000, ApJ, 542, 914
Xia X. Y. et al., 2012, ApJ, 750, 92
Xu C. K. et al., 2014, ApJ, 787, 48
Young J. S. et al., 1995, ApJS, 98, 219
Zaragoza-Cardiel J., Beckman J., Font J., Rosado M., Camps-Fariña A., Borlaff A., 2017, MNRAS, 465, 3461
Zhao Y. et al., 2016, ApJ, 820, 118

APPENDIX A: CO LINE RATIOS

In this section, we show the CO luminosity ratios, both with denominators the CO(1–0) and the CO(6–5) luminosity. The CO(1–0) luminosities have been corrected to take into account only the emission up to $r = 250$ pc from the centre of the galaxies (with equation 1). First, we plot the luminosity ratios against the FUV flux G_0 and the X-ray flux F_X, fitting the points with a regression line, respectively as in Figs 3 and 4. The details can be found in Sections 5.1 and 5.2. Secondly, we plot the same points but with the CLOUDY models at different gas densities superimposed, as in Fig. 5, and as explained in detail in Section 5.3.

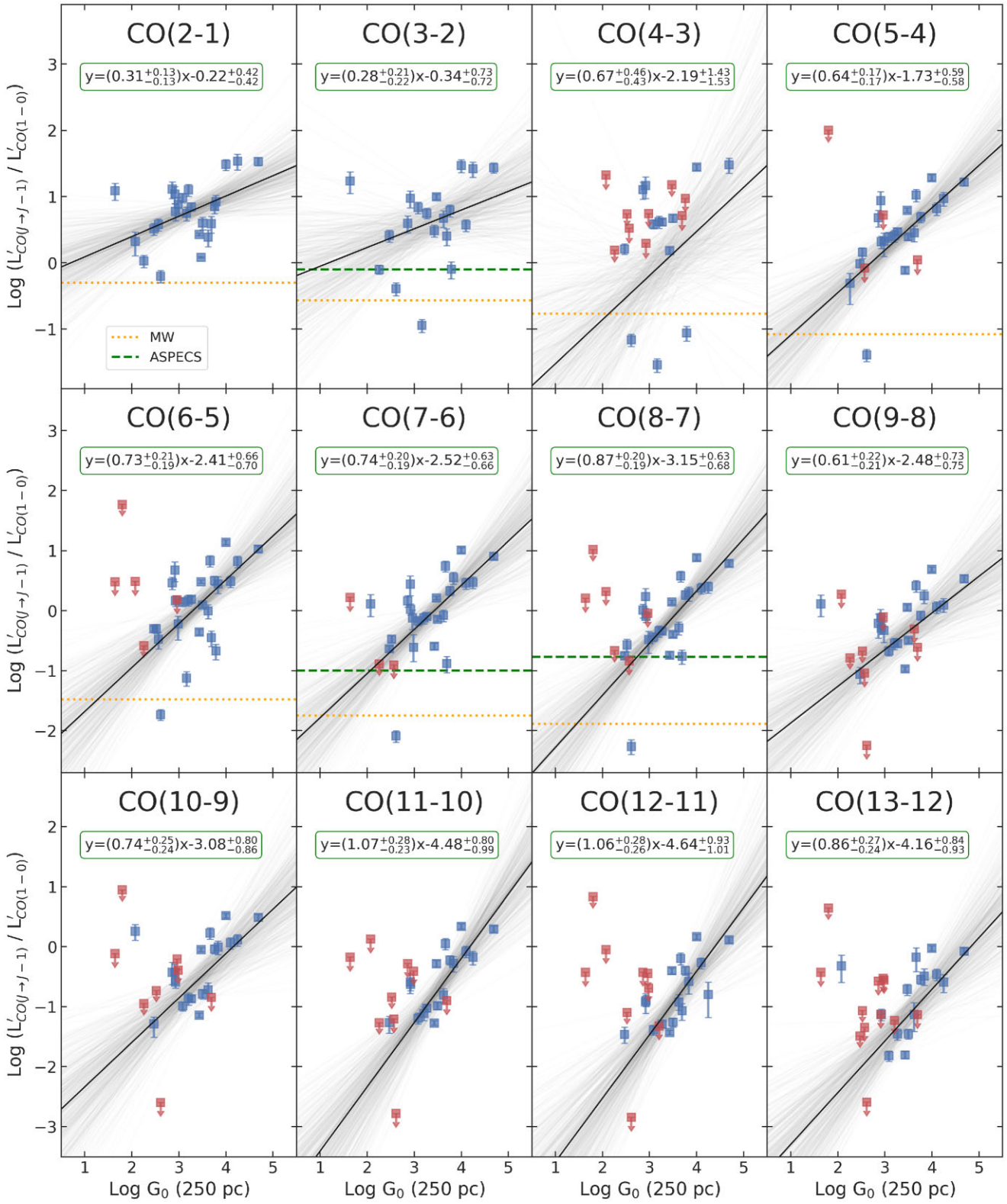

Figure A1. CO line ratios, with respect to the CO(1–0) line, versus G_0. The x-axis is the Habing field G_0 (for $r = 250$ pc). The y-axis is the luminosity ratio $L'_{CO(J\rightarrow J-1)}/L'_{CO(1\rightarrow 0)}$ to the nuclear ($r = 250$ pc) fraction of CO(1–0). The luminosities L' are in units of K km s^{-1} pc^{-2}, and J is indicated on the top of each panel. Blue squares indicate 3σ detections in both lines; red squares with downward arrow indicate less than 3σ in the higher-J line (i.e. censored data). The lines are regression fits to the observed data: solid black line is the median Linmix regression, thin shaded green lines show fits drawn from the posterior distribution of Linmix regression. When available, the Milky Way (dotted orange line, data from Fixsen et al. 1999) and the ASPECS AGN (green dashed line, data from Boogaard et al. 2020) CO ratios are also shown.

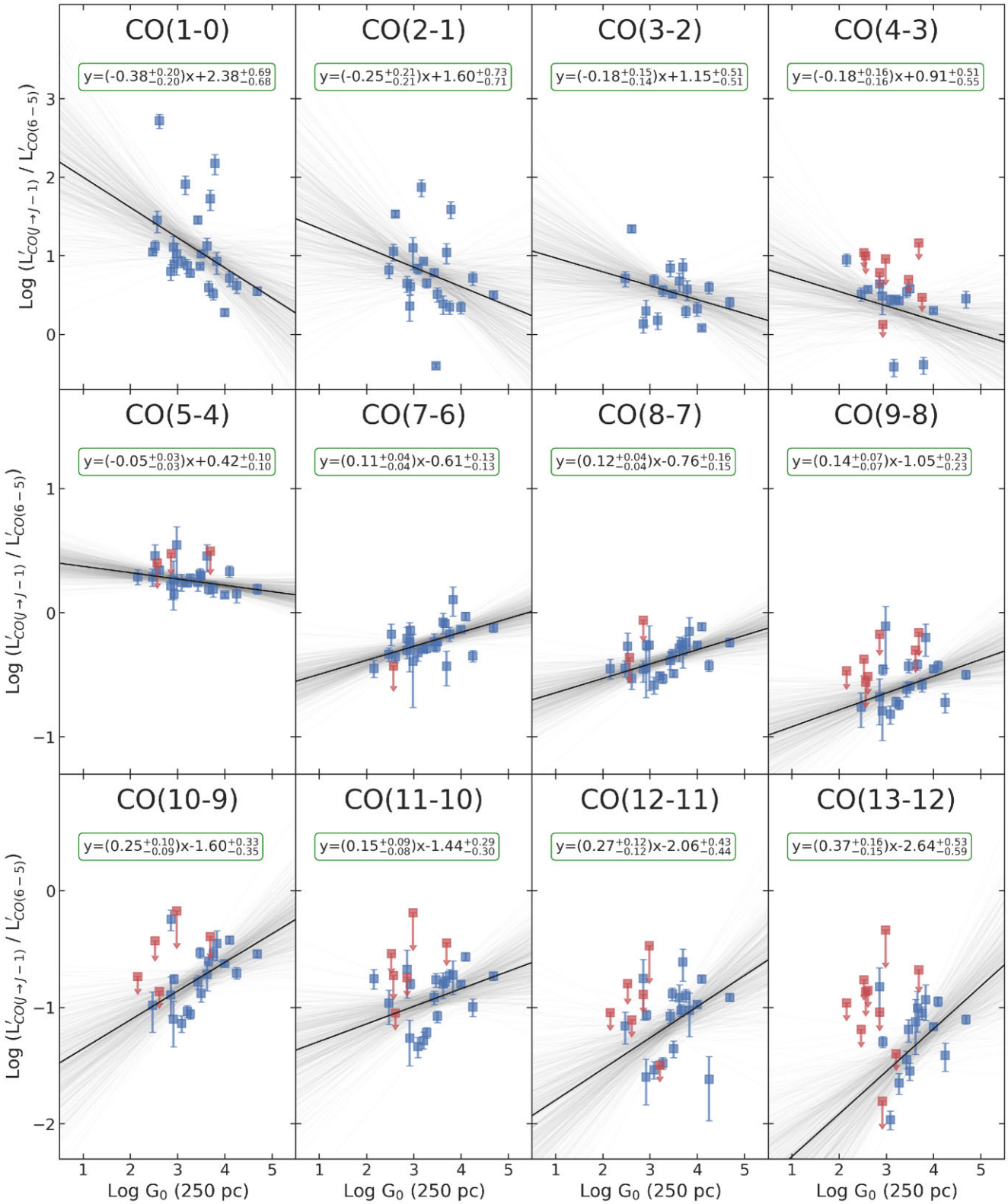

Figure A2. CO line ratios, with respect to the CO(6–5) line, versus G_0. The x-axis is the Habing field G_0 (for $r = 250$ pc). The y-axis is the luminosity ratio $L'_{CO(J\rightarrow J-1)}/L'_{CO(6\rightarrow 5)}$ to the CO(6–5) line. Data points and lines are described in Fig. A1.

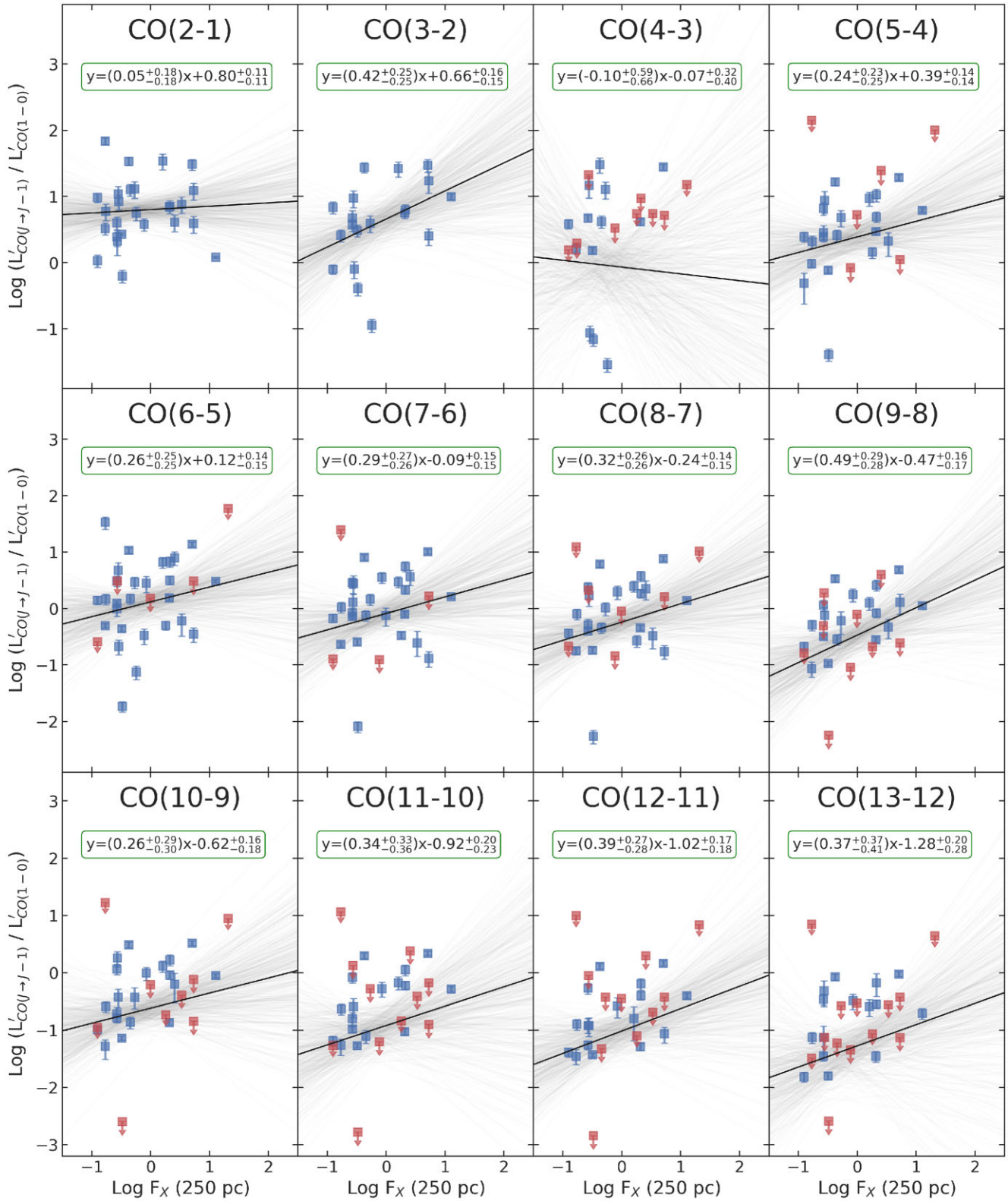

Figure A3. CO line ratios, with respect to the CO(1–0) line, versus F_X. The x-axis is F_X (for $r = 250$ pc), in units of erg s^{-1} cm^{-2}. The y-axis is the luminosity ratio $L'_{CO(J\to J-1)}/L'_{CO(1\to 0)}$ to the nuclear ($r = 250$ pc) fraction of CO(1–0). Data points and lines are described in Fig. A1.

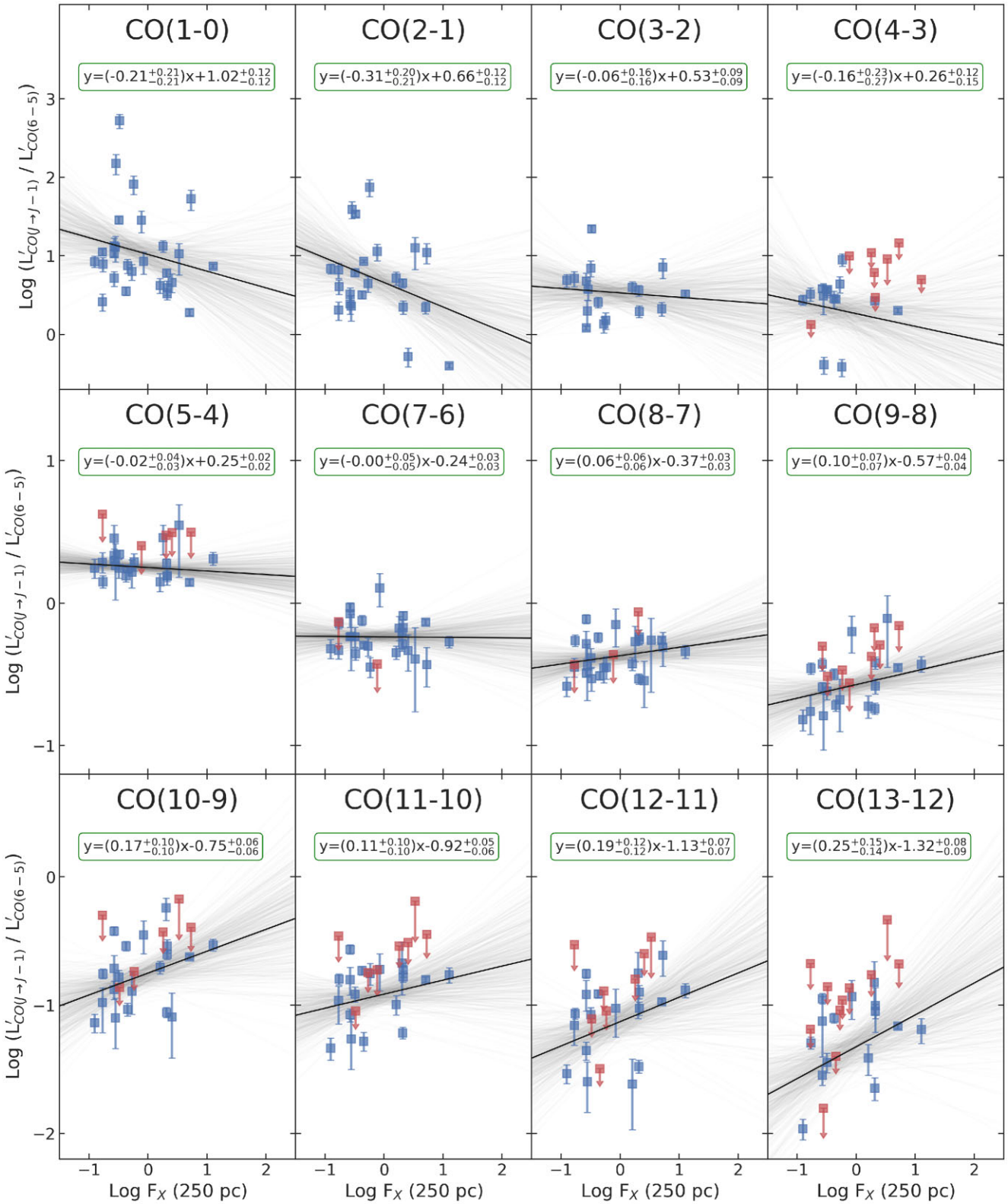

Figure A4. CO line ratios, with respect to the CO(6–5) line, versus F_X. The x-axis is F_X (for $r = 250$ pc), in units of erg s^{-1} cm^{-2}. The y-axis is the luminosity ratio $L'_{CO(J\rightarrow J-1)}/L'_{CO(6\rightarrow 5)}$ to the CO(6–5) line. Data points and lines are described in Fig. A1.

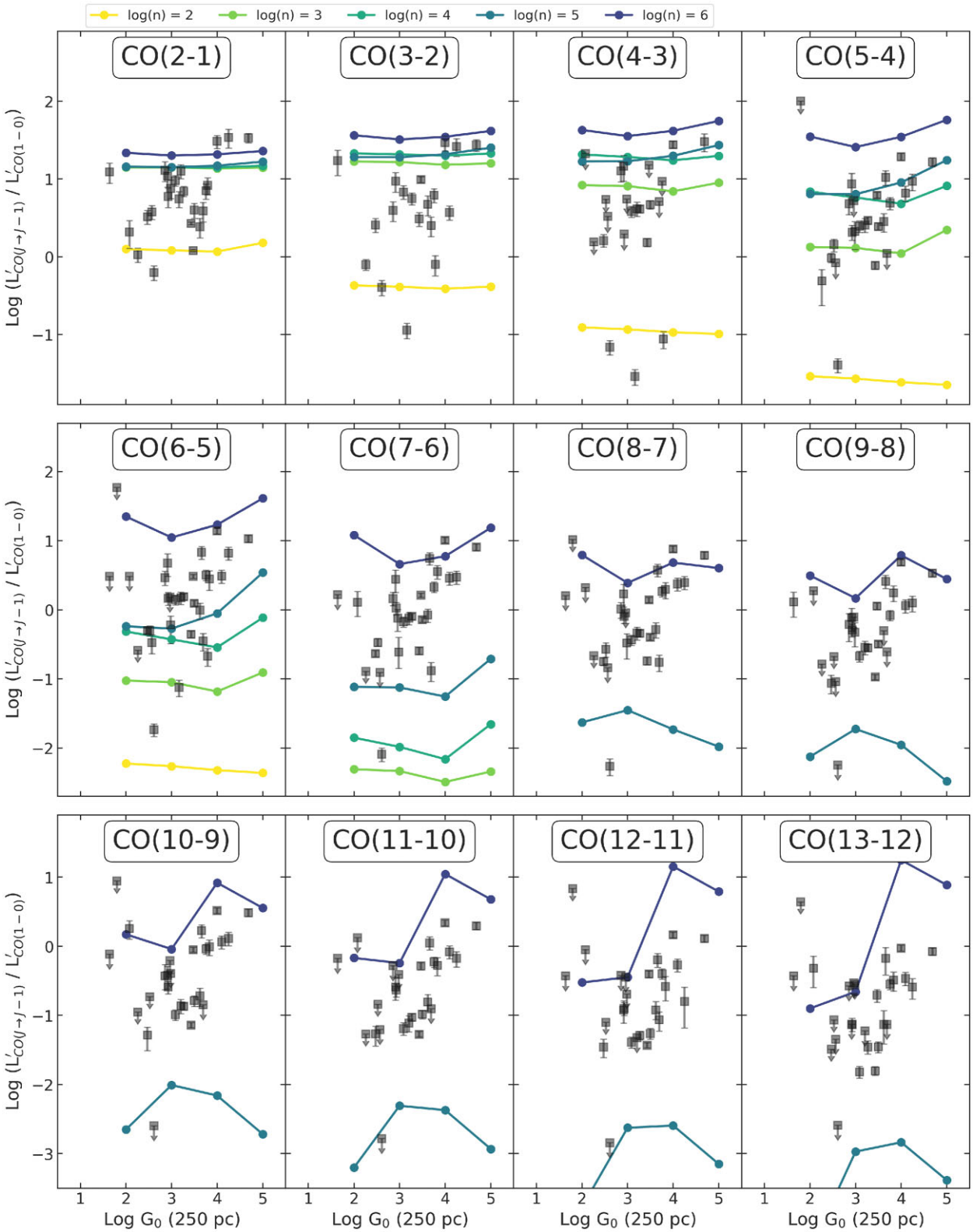

Figure A5. CO line ratios, with respect to the CO(1–0) line, versus G_0. The x-axis is the Habing field G_0 (for $r = 250$ pc). The y-axis is the luminosity ratio $L'_{\mathrm{CO}(J\rightarrow J-1)}/L'_{\mathrm{CO}(1\rightarrow 0)}$ to the nuclear ($r = 250$ pc) fraction of CO(1–0). The luminosities L' are in units of K km s^{-1} pc^{-2}, and J is indicated on the top of each panel. Squares with downward arrow indicate less than 3σ detections in the higher-J line (i.e. censored data). The coloured overplotted lines are CLOUDY numerical models at different gas densities, namely 10^2 (yellow), 10^3 (light green), 10^4 (dark green), 10^5 (blue), and 10^6 (purple) cm^{-3}.

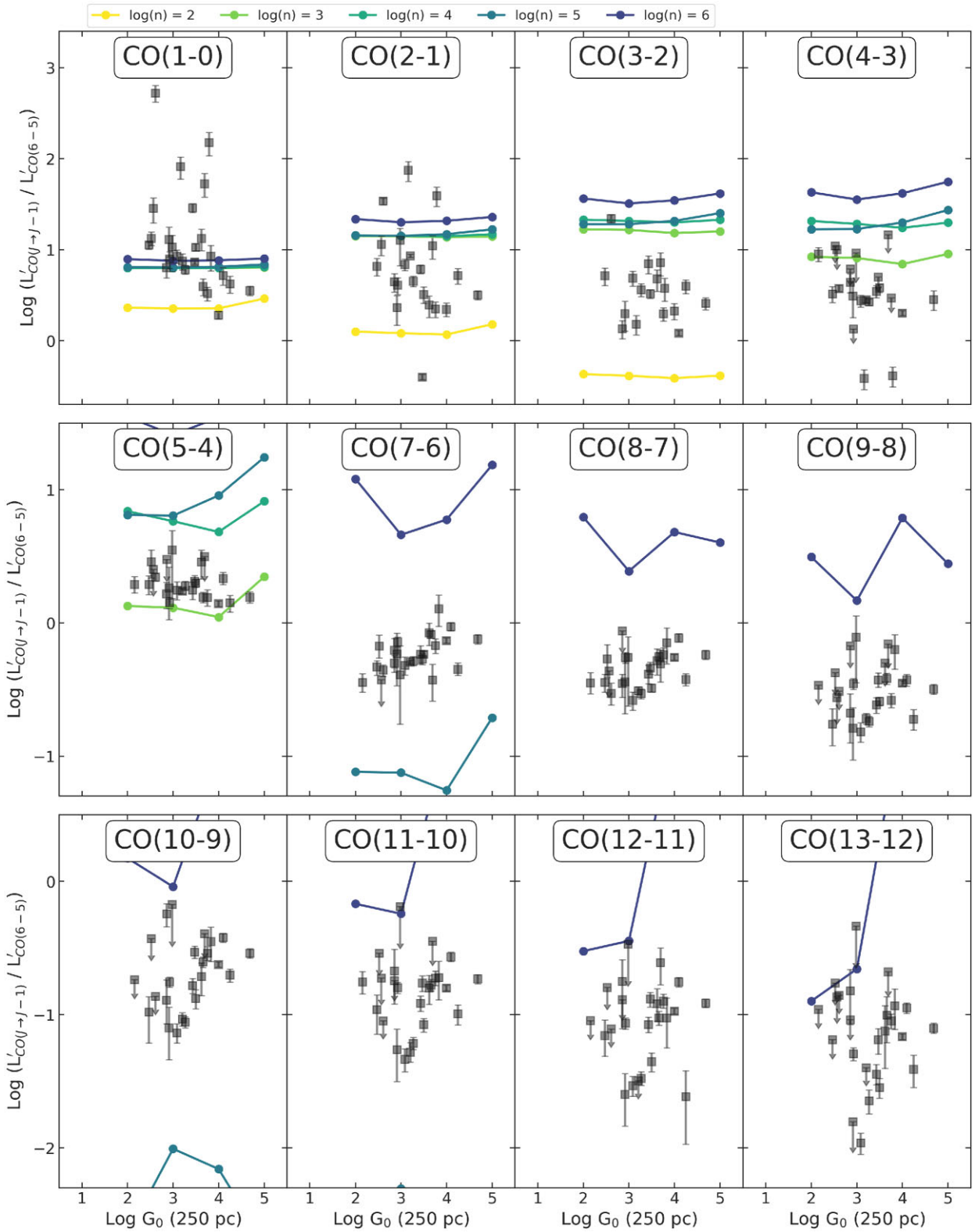

Figure A6. CO line ratios, with respect to the CO(6–5) line, versus G_0. The x-axis is the Habing field G_0 (for $r = 250$ pc). The y-axis is the luminosity ratio $L'_{\mathrm{CO}(J\rightarrow J-1)}/L'_{\mathrm{CO}(6\rightarrow 5)}$ to the CO(6–5) line. Data points and lines are described in Fig. A5.

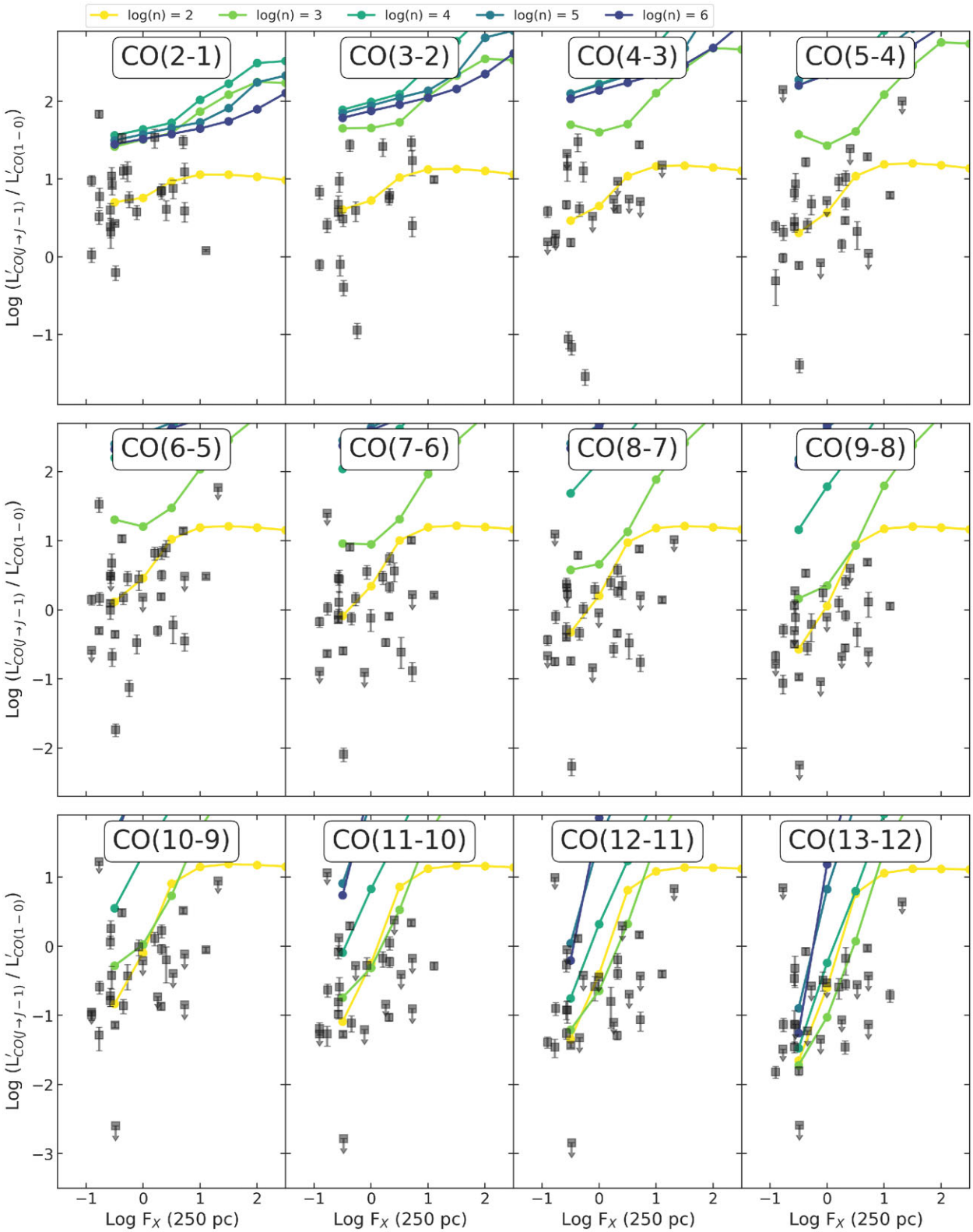

Figure A7. CO line ratios, with respect to the CO(1–0) line, versus F_X. The x-axis is F_X (for $r = 250$ pc), in units of erg s^{-1} cm^{-2}. The y-axis is the luminosity ratio $L'_{\mathrm{CO}(J\rightarrow J-1)}/L'_{\mathrm{CO}(1\rightarrow 0)}$ to the nuclear ($r = 250$ pc) fraction of CO(1–0). Data points and lines are described in Fig. A5.

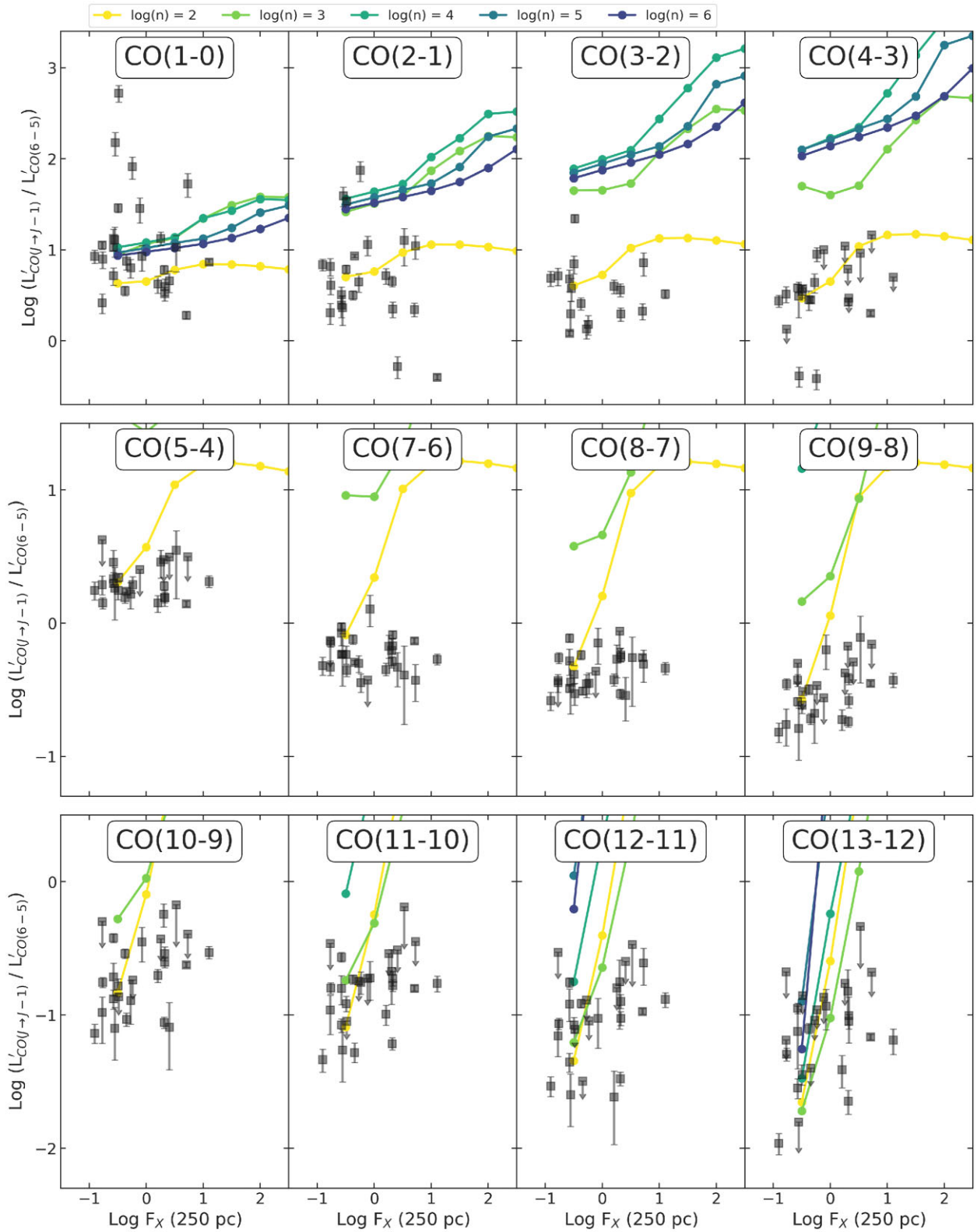

Figure A8. CO line ratios, with respect to the CO(6–5) line, versus F_X. The x-axis is F_X (for $r = 250$ pc), in units of erg s^{-1} cm^{-2}. The y-axis is the luminosity ratio $L'_{\mathrm{CO}(J\rightarrow J-1)}/L'_{\mathrm{CO}(6\rightarrow 5)}$ to the CO(6–5) line. Data points and lines are described in Fig. A5.

APPENDIX B: CO(6–5) ATLAS

In this section, we present the rest (in addition to Fig. 1) of the images of CO(6–5) emission for our sample galaxies. All the CO(6–5) data cubes are from the ALMA Archive, already calibrated, cleaned, and when available, primary-beam corrected. Using CASA 5.6 (McMullin et al. 2007), we produce the moment 0 map from the data cubes with the task `immoments`. We then plot the ALMA CO(6–5) contours over the optical image of the galaxy.

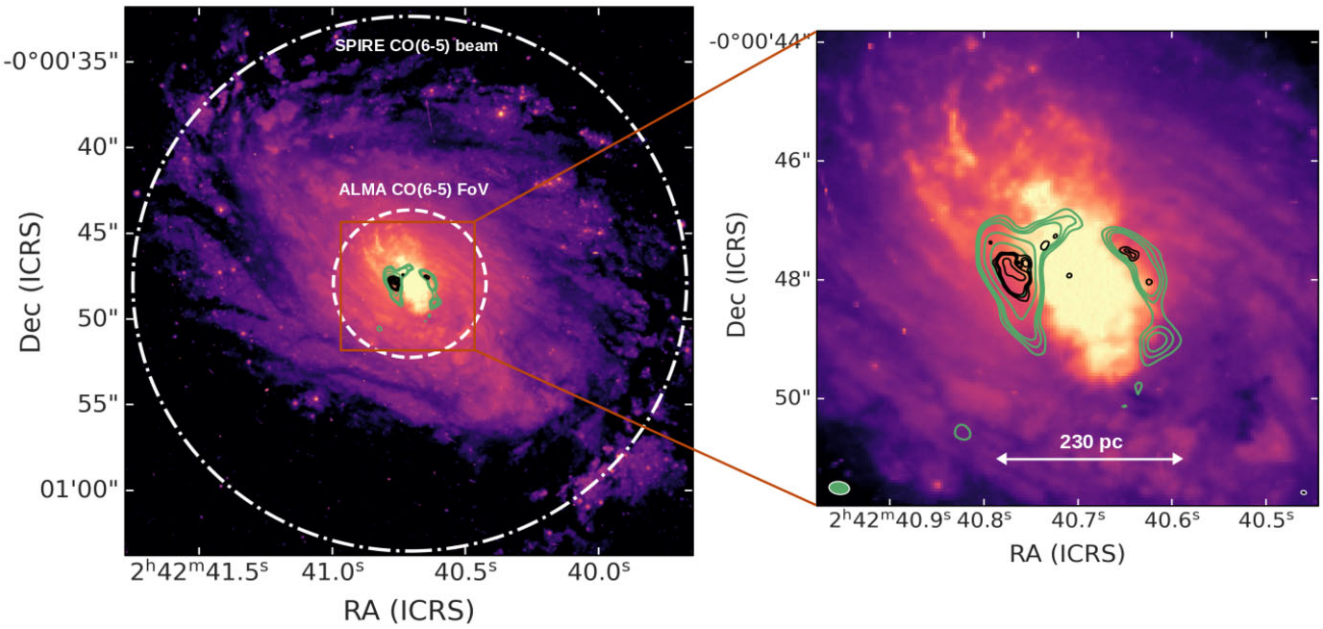

Figure B1. *Left-hand panel: HST* WFPC2 F606W image of NGC 1068 (from Malkan et al. 1998) with superimposed the contours of two ALMA CO(6–5) observations, in green at the resolution of 250 mas (project 2011.0.00083.S, PI: García-Burillo), in black of 90 mas (project 2013.1.00014.S, PI: Elitzur). Both the contours are at the respective (3, 4, 5, 10, 20) $\times\sigma$, where $\sigma = 6.2$ Jy beam^{-1} km s^{-1} for the green lines and $\sigma = 1.1$ Jy beam^{-1} km s^{-1} for the black lines. The inner white dashed circle indicates the FoV of both ALMA observations, with a radius of 4.3 arcsec (∼340 pc), while the outer dash–dotted circle represents the *Herschel*/SPIRE-FTS beam FWHM for CO(6–5) observations, with a 15.″6 radius. *Right-hand panel:* zoom of the inner 670 pc. Restored ALMA beams of the 250 and 90 mas images are shown as ellipses with white edges, at the bottom left (with the green area) and right (with the black area), respectively. The 250 mas ALMA image has not been primary-beam corrected.

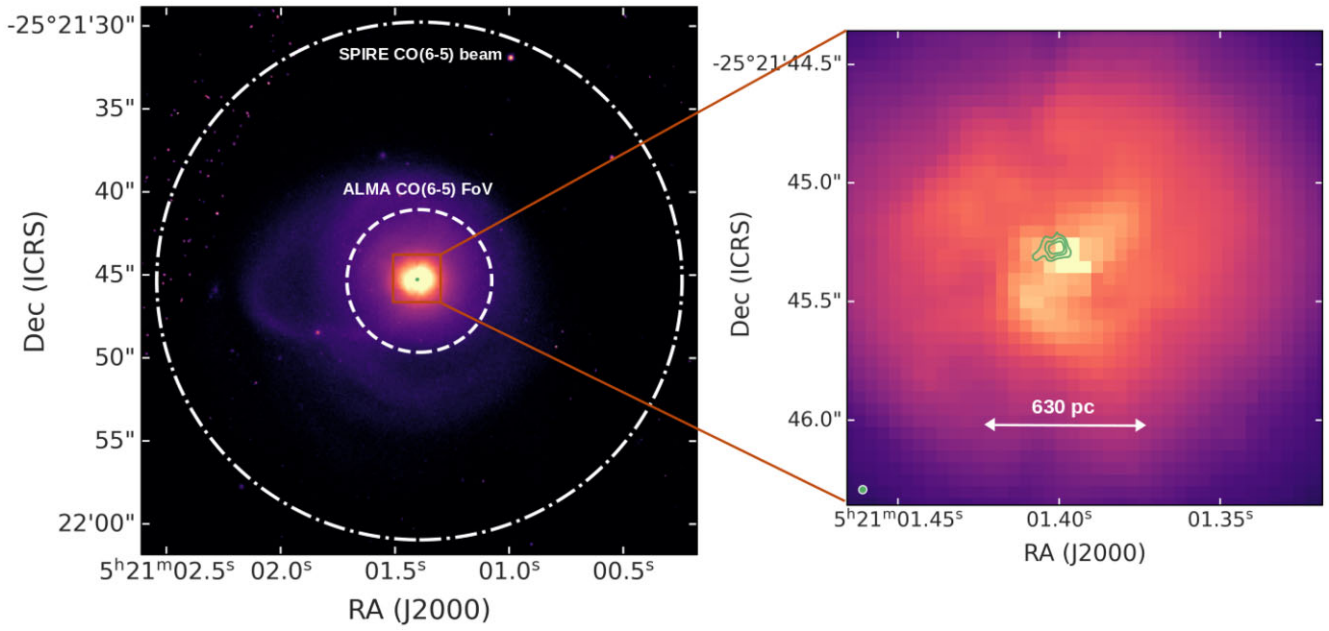

Figure B2. *Left-hand panel: HST* ACS F814W image of IRAS F05189–2524 (from Evans 2005), with superimposed, in green, the contours of ALMA CO(6–5) moment 0 at the resolution of 40 mas (project 2016.1.01223.S, PI: Baba). The contours are drawn at (3, 4, 5, 10, 20) $\times\,\sigma$, where $\sigma = 0.55$ Jy beam^{-1} km s^{-1}. The inner white dashed circle indicates the FoV of both ALMA observations, with a radius of 4.3 arcsec (∼3.6 kpc), while the outer dash–dotted circle represents the *Herschel*/SPIRE-FTS beam FWHM for CO(6–5) observations, with a 15.″6 radius. *Right-hand panel:* zoom of the inner 1.7 kpc. The restored ALMA beam is shown as a green ellipse with white edges at the bottom left.

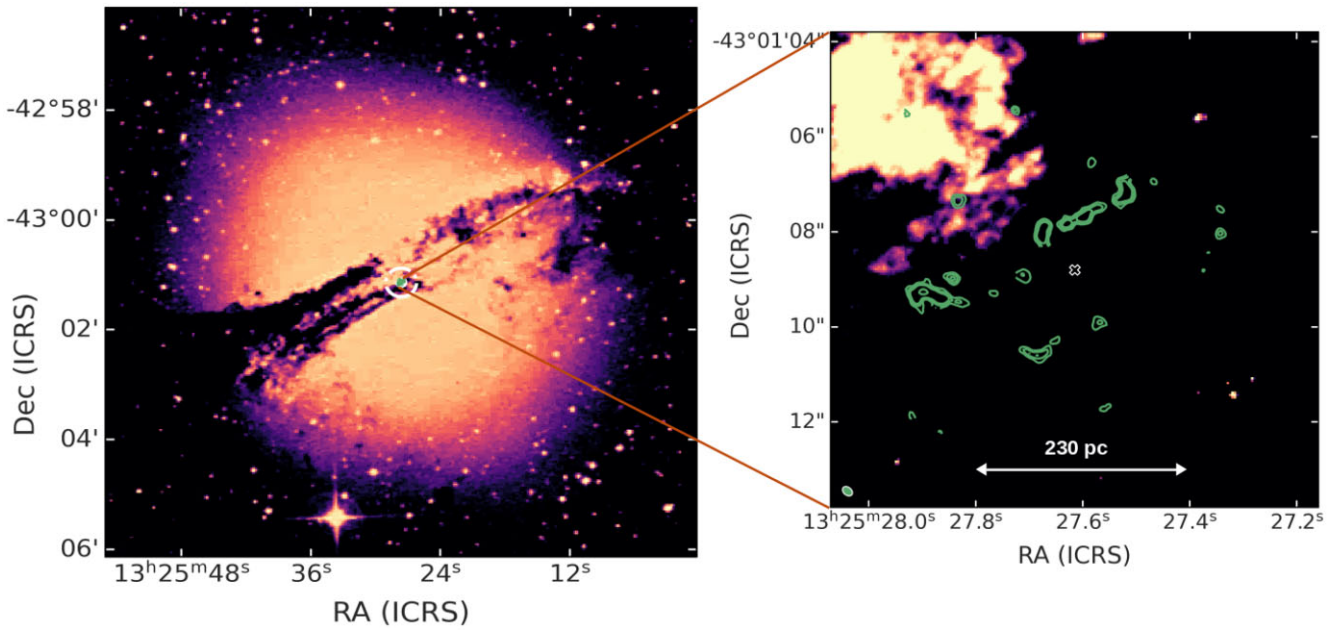

Figure B3. *Left-hand panel:* DSS-2 *B*-band image of NGC 5128. The inner white dashed circle indicates the FoV of both ALMA observations, with a radius of 4.3 arcsec (∼160 pc), while the outer dash–dotted circle represents the *Herschel*/SPIRE-FTS beam FWHM for CO(6–5) observations, with a 15.6 arcsec radius. *Right-hand panel:* Zoom of the inner 380 pc, with *HST* WFPC2 F555W image of NGC 5128 (from Marconi et al. 2000) in the background, with superimposed, in green, the contours of ALMA CO(6–5) moment 0 at the resolution of 170 mas (project 2012.1.00225.S, PI: Espada). The contours are drawn at (3, 4, 5, 10, 20) $\times\,\sigma$, where $\sigma = 0.42$ Jy beam^{-1} km s^{-1}. The restored ALMA beam is shown as a green ellipse with white edges at the bottom left. A 'X' marker, black with white edges, indicates the centre of the galaxy.

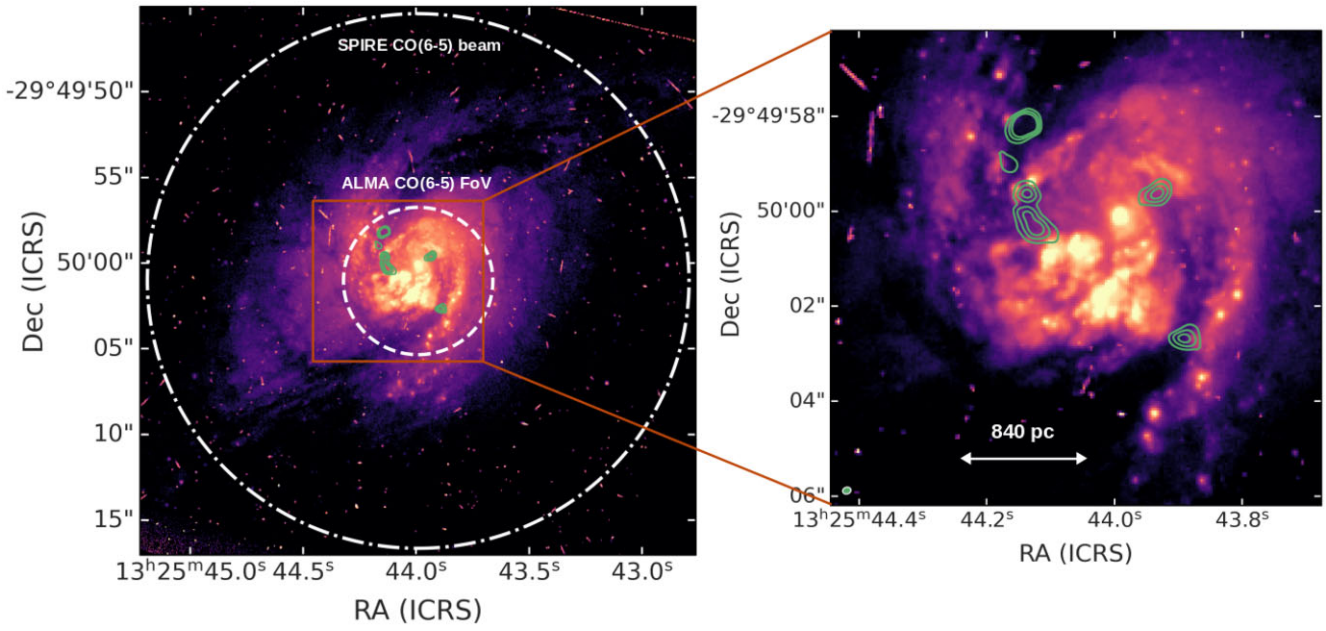

Figure B4. *Left-hand panel: HST* WFPC2 F606W image of NGC 5135 (from Malkan et al. 1998), with superimposed, in green, the contours of ALMA CO(6–5) moment 0 at the resolution of 170 mas (project 2013.1.00524.S, PI: Lu). The contours are drawn at (3, 4, 5, 10, 20) $\times\,\sigma$, where $\sigma = 1.2$ Jy beam^{-1} km s^{-1}. The inner white dashed circle indicates the FoV of both ALMA observations, with a radius of 4.3 arcsec (∼1.2 kpc), while the outer dash–dotted circle represents the *Herschel*/SPIRE-FTS beam FWHM for CO(6–5) observations, with a 15.6 arcsec radius. *Right-hand panel:* Zoom of the inner 2.5 kpc. The restored ALMA beam is shown as a green ellipse with white edges at the bottom left.

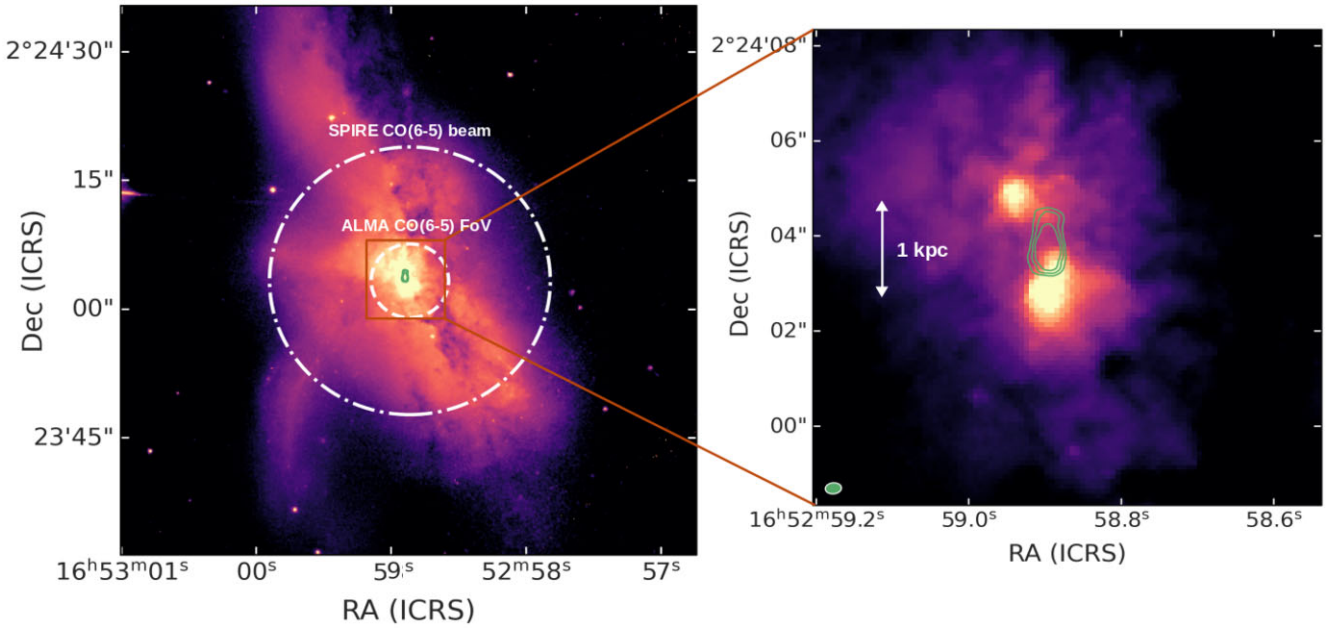

Figure B5. *Left-hand panel: HST* WFPC2 F814W image of NGC 6240 (from Gerssen et al. 2004), with superimposed, in green, the contours of ALMA CO(6–5) moment 0 at the resolution of 250 mas (project 2015.1.00658.S, PI: Rangwala). The contours are drawn at (3, 4, 5, 10, 20) $\times\,\sigma$, where $\sigma = 29$ Jy beam^{-1} km s^{-1}. The inner white dashed circle indicates the FoV of both ALMA observations, with a radius of 4.3 arcsec (∼2.1 kpc), while the outer dash–dotted circle represents the *Herschel*/SPIRE-FTS beam FWHM for CO(6–5) observations, with a 15.″6 radius. *Right-hand panel:* Zoom of the inner 4.5 kpc. The restored ALMA beam is shown as a green ellipse with white edges at the bottom left.

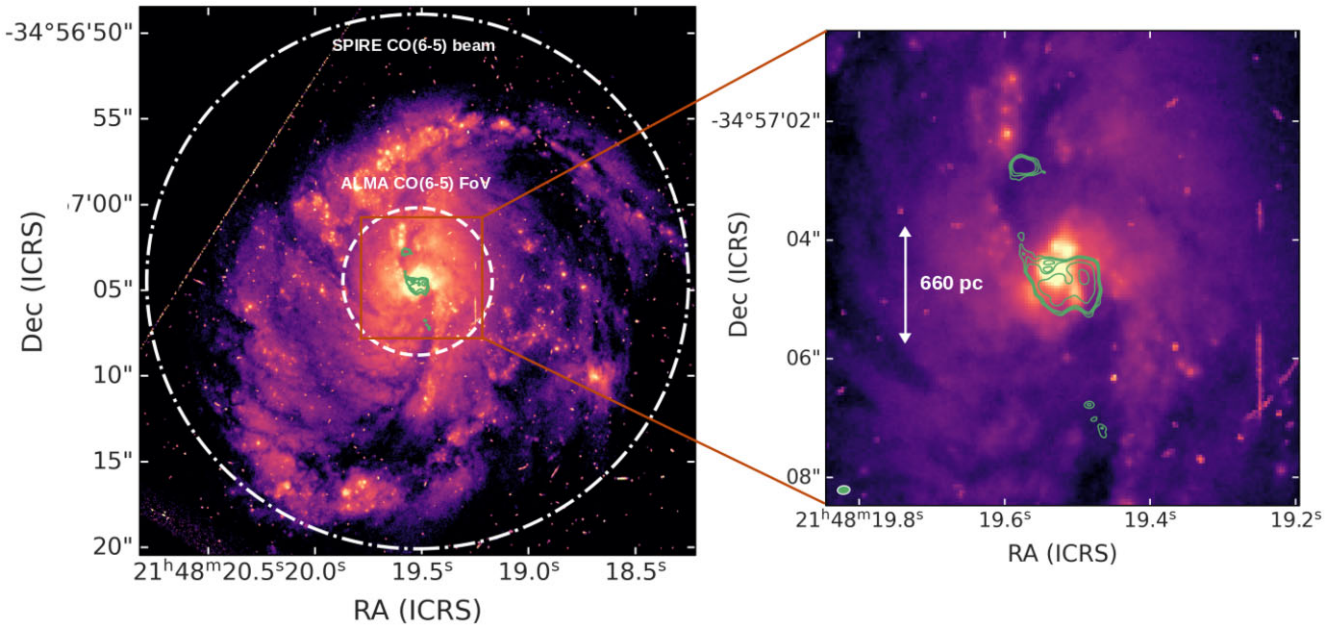

Figure B6. *Left-hand panel: HST* WFPC2 F606W image of IRAS F05189–2524 (from Malkan et al. 1998), with superimposed, in green, the contours of ALMA CO(6–5) moment 0 at the resolution of 180 mas (project 2013.1.00524.S, PI: Lu). The contours are drawn at (3, 4, 5, 10, 20) $\times\,\sigma$, where $\sigma = 1.5$ Jy beam^{-1} km s^{-1}. The inner white dashed circle indicates the FoV of both ALMA observations, with a radius of 4.3 arcsec (∼1.4 kpc), while the outer dash–dotted circle represents the *Herschel*/SPIRE-FTS beam FWHM for CO(6–5) observations, with a 156 radius. *Right-hand panel:* Zoom of the inner 2.3 kpc. The restored ALMA beam is shown as a green ellipse with white edges at the bottom left. This ALMA image has not been primary-beam corrected.

This paper has been typeset from a TEX/LATEX file prepared by the author.